Spring 2018

Brush-First Synthesis of Acid-Labile Star-Like Poly(ethylene glycol) Nanogels for Drug Delivery Applications

Julian Grundler
Rollins College, jgrundler@rollins.edu

Brush-First Synthesis of Acid-Labile Star-Like Poly(ethylene glycol) Nanogels for Drug Delivery Applications

Julian Grundler

May 2018

Faculty Advisor: Dr. Ellane J. Park

Department of Chemistry, Rollins College, Winter Park, FL, United States.

Acknowledgements

I would like to express my deep gratitude to my research advisor and mentor Dr. Ellane Park who has always supported me in my academic and research pursuits. Her enthusiasm for chemistry and inspiring nature, motivated me to challenge my understanding of chemistry in and outside the lab as well as shaped my interest in nanoscience.

I would also like to thank Dr. Jeremiah Johnson at Massachusetts Institute of Technology for giving me the opportunity to continue the collaboration with his research group on this project. In particular, I thank Hung Nguyen for performing GPC measurements, as well as being a helpful resource for any synthesis-related questions and Dr. Matthew Golder for introducing me to the BASP synthesis and inspiring the idea behind this project.

I would like to express my appreciation to the members of my Rollins thesis committee, Dr. James Patrone and Dr. Pedro Bernal, for their contributions and advice. Furthermore, I thank Dr. Habgood for granting me access to her lab and glove box.

Finally, I would like to dedicate my thesis to my family and friends. They have always helped me get through stressful times and supported me in my academic and personal journey.

Table of Contents

1. Abstract

The development of multidrug-conjugated polymeric nanoparticles for drug delivery applications promises more effective forms of cancer therapy based on the target-specific, triggered release of therapeutic agents at the tumor site. Discrimination between healthy tissue and tumor cells can be achieved by exploiting the characteristics of the mildly acidic tumor microenvironment. While previous studies showed the potential of acid-responsive polymeric nanoparticles, low drug-loading and failure to release drugs in response to tumor-specific pH conditions remain a challenge in drug delivery and synthetic chemistry.

This work presents the synthesis of acid-degradable star-like polymeric nanogels that allow high drug-loading and acid-triggered core degradation in tumor tissue based on the brush-first ring-opening metathesis polymerization (ROMP) method. These brush-arm star polymer (BASP) nanogels are composed of two monomers: (1) poly(ethylene glycol) (PEG) norbornene-terminated macromonomer providing biocompatible and water-soluble features and (2) the acid-cleavable acetal-based cross-linker enabling acid-triggered core degradation. After brush formation of PEG macromonomer resulting in the hydrophilic shell, a mixture of PEG macromonomer and cross-linker initiates the formation of the gel-like core via cross-linking.

BASP nanogels were successfully synthesized using various ratios of cross-linker to PEG macromonomer. Characterization via gel permeation chromatography (GPC) confirmed the formation of mostly monomodal BASP nanogels with decreasing MW as the amount of PEG macromonomer is increased. Additional GPC analysis of acid degraded BASP nanogels suggests that the macromonomer increases the steric hindrance during cross-coupling and core formation resulting in smaller BASP nanogels. Furthermore, fluorescence studies show the successful loading of a fluorescein dye into BASP nanogel.

2. Introduction

2.1. Conventional Cancer Therapy

As the second leading cause of death globally after cardiovascular disease, cancer is responsible for nearly 1 in 6 deaths according to the World Health Organization.[1] The American Cancer Society estimates that approximately 41 out of 100 men and 38 out of 100 women in the US will be diagnosed with some form of cancer during their lifetime.[2] For decades, the standard procedure for treating tumor-forming cancer types involved the administration of chemotherapy with or without initial local forms of therapy such as surgery and radiation therapy.

While the survival rate of most cancer types has gradually improved with the development of more effective chemotherapeutic agents, severe side effects that typically accompany chemotherapy remain a major challenge in cancer therapy as they considerably lower the maximum tolerable dose (MTD). The basic principle of chemotherapy relies on cytotoxic agents that destroy tumor cells by inhibiting cell proliferation.[3] However, as chemotherapeutic agents do not have the ability to effectively discriminate between healthy cells and tumor cells, they readily accumulate in rapidly dividing healthy tissue resulting in unfavorable side effects. More effective strategies of drug delivery have garnered great attention in overcoming the limitations of conventional chemotherapy.

2.2. Drug Delivery

Conventional free drugs used in chemotherapy most often suffer from unfavorable pharmacological and physiochemical properties limiting their therapeutic efficacy. Furthermore, poor solubility of hydrophobic drugs as well as unfavorable pharmacokinetics negatively affect the blood circulation lifetime presenting a major challenge in the design of therapeutic agents.

However, in the context of chemotherapy involving highly cytotoxic agents, poor biodistribution and lack of selectivity of free drugs may pose even greater risk to the patient.

Recent efforts in the field of cancer research have focused on developing methods to reduce off-target toxicity of anti-cancer drugs by conjugating drug molecules to biocompatible carriers that provide favorable pharmacological characteristics. Selective accumulation in tumor tissue is generally achieved via two mechanisms, passive targeting and active targeting, relying on the affinity of the drug-carrier for tumor cells. At the target site, drugs are selectively released from the drug-carrier complex and interact with the target cell without affecting peripheral healthy tissue.

2.2.1. Passive Targeting

Passive targeting is based on the transport of the drug-carrier complex through the bloodstream to the target site. In the absence of specific interactions between nanocarrier and tumor cell, selective accumulation in tumor tissue is achieved through the enhanced permeability and retention (EPR) effect. Rapidly growing tumor cell generate new blood vessels via angiogenesis to meet their increased nutritional needs (Figure 1d).[4] Based on the tumor type, these blood vessels exhibit abnormal leakage with gap sizes between 100 nm to 2 µm, as well as a poor lymphatic drainage (Figure 1b).[5,6] This results in a higher retention ability and accumulation of nanocarriers in cancerous tissue.[7]

As no specific targeting moiety is required for passive targeting to occur, the EPR effect is commonly exploited in the development of nanocarriers for cancer therapy. However, the limited control of targeting and slow accumulation in tumor tissue requires nanocarriers with particularly long half-lives in order for the drug to accumulate in significant concentrations.[8] Drug delivery based on passive targeting is further complicated by the high tumor interstitial fluid pressure (IFP) resulting in decreased uptake and inhomogeneous distribution.[9] A study conducted by Matsumura

et al. suggests that EPR effect may only offer a modest increase in delivery (i.e., less than 2-fold) compared to normal tissue.[10,11] Moreover, only certain tumor types exhibit EPR after they have reached a sufficient size, significantly limiting the therapeutic use of passive targeting.
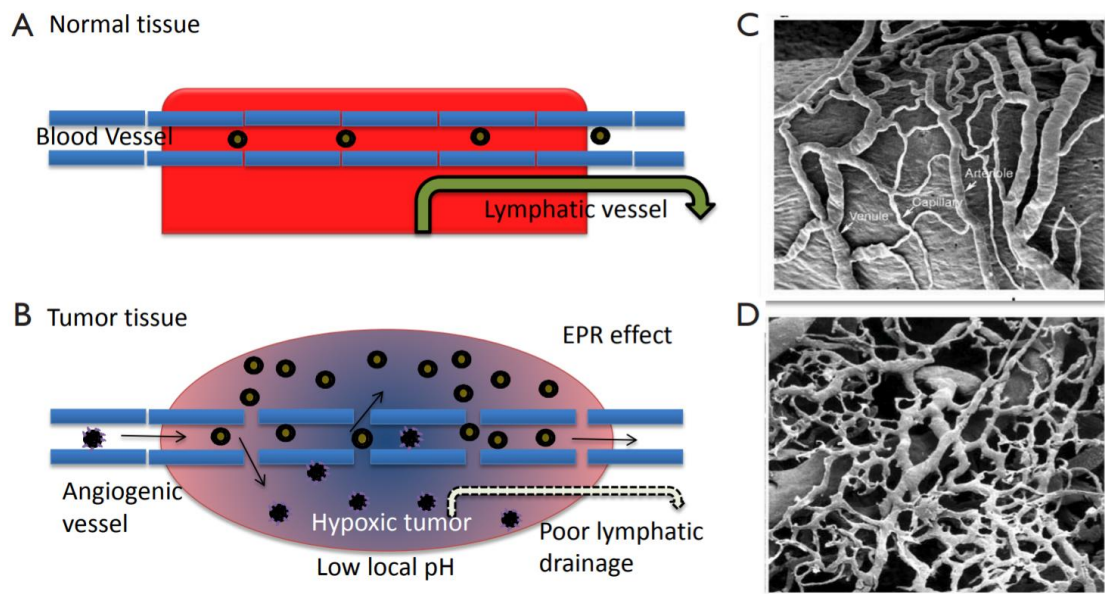
Figure 1. Illustration of EPR effect and its impact on nanoparticle delivery.[12] Scheme (A) represents the microvasculature of normal tissue compared to tumor tissue in (B) where black circles represent nanocarriers. Scanning electron microscope (SEM) image (C) showing hierarchical microvasculature in normal rat carotid sinus, whereas (D) depicts the microvasculature in mice lacking an organized arrangement of blood vessels.

2.2.2. Active Targeting

Active targeting has the potential to overcome the limitations of passive targeting providing a promising method for reducing the off-target toxicity of chemotherapeutic agents. Discrimination between cancer tissue and healthy tissue relies on the overexpression of specific surface receptor on tumor cells. In active targeting, nanocarriers are typically conjugated with peripheral binding epitopes such as antibody fragments or carbohydrates that selectively bind to endocytosis-prone receptors enabling enhanced cellular internalization. Well-studied attractive targets for active targeting include the transferrin receptor, the folate receptor, and glycoproteins.[13–15] While studies have shown the increased therapeutic efficiency of drug-loaded nanoparticles employing active targeting with up to 30-fold increase in delivery relative to normal tissue, the conjugation of

targeting moieties to nanocarriers still remains a formidable challenge.[16–18] As a result of conjugation, nanocarrier-bound targeting moieties may exhibit decreased receptor affinity compared to the free circulating equivalent.[4]

2.2.3. Drug Release Mechanism

While active and passive targeting may prevent the accumulation of cytotoxic agents in healthy tissue, the mechanism of drug release is just as essential for reducing the side effects of conventional chemotherapy. In general, drug release is initiated in response to internal and external stimuli that enable the localized release of therapeutic agents at the target site in a controlled and sustained manner. Internal stimuli are based on the unique characteristics of tumor tissue enabling self-controlled drug release without external intervention.

A promising approach for the selective drug release in tumor cells is a pH-triggered release mechanism exploiting the mildly acidic tumor microenvironment (pH ~ 6.0).[19] As tumor cells rely on increased glycolysis for their rapid proliferation, they produce acidic lactate even under aerobic conditions according to the Warburg effect ultimately lowering the pH inside the tumor.[20] Other internal approaches focus on the increased reduction potential in the cytosol caused by high concentrations of glutathione (GSH) enabling the potential use of disulfide linker.[21]

Drug release triggered by external stimuli provides an external spatial and temporal control of the release mechanism. Photocleavage in response to UV-irradiation, in particular, offers a well-established method for the controlled release of free drug molecules from nanocarriers. Furthermore, the combination of multiple release mechanisms in a multi-stimuli responsive nanocarrier may allow for even greater control while preventing premature drug leakage more effectively.[22]

2.2.4. Types of Nanocarrier

The type of nanocarrier utilized in drug delivery is the determining factor in controlling the pharmacological properties of the drug-carrier complex. Nanoconjugates involving metallic and polymeric nanoparticles, liposomes, micelles, and antibodies as the carrier (Figure 2) have shown potential in improving the efficacy of existing chemotherapy while reducing adverse side effects.[23] Inorganic nanoparticles offer unique physical and biological characteristics such as high stability, magnetic, and optical-electronic properties based on their metallic constituents. Furthermore, controlling the crystal growth enables the synthesis of homogeneous and heterogenous inorganic nanoparticle typically made out of gold, silver, iron oxide, or copper in various shapes and sizes.[24,25] While certain types of inorganic nanoparticles have gained increasing popularity as high-performance imaging agents, concerns about their biocompatibility and lack of renal clearance have limited their usage as nanocarriers in cancer research.[26,27]

Liposomal nanocarriers, however, have received broad attention as the first nanomedicine in FDA clinical trials followed by the approval of several liposomal formulations for cancer treatment.[28] Liposomes typically consist of a self-assembled phospholipid bilayer encapsulating the drug preventing undesirable interactions. While liposomal carriers present a well-established tool in nanotherapeutics due to their straightforward synthesis and facile incorporation of targeting ligands, their rapid clearance results in unfavorably short circulation half-lives.[28] In fact, a recent study by Petersen *et. al*. suggests that liposomal formulations do not increase the overall survival of cancer patients compared to the conventional free drug.[29]
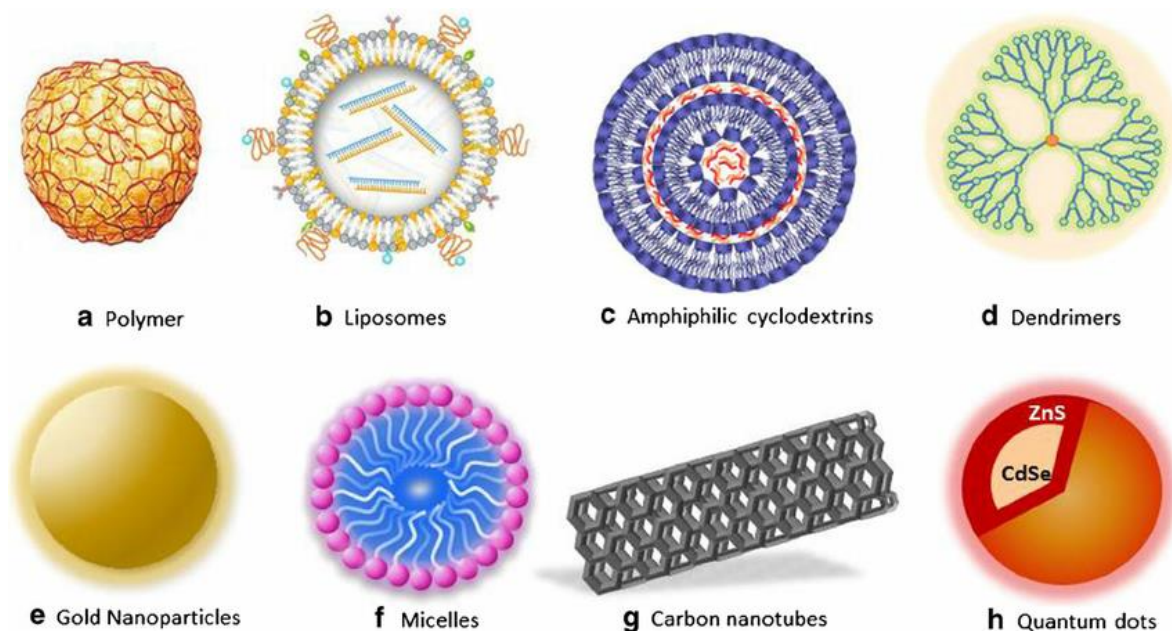
Figure 2. Different types of nanocarriers used for drug delivery applications.[30]

Closely related to the concept of liposomal transport are polymeric micelles typically containing amphiphilic block copolymers that self-assemble into spheres with hydrophobic cores and hydrophilic shells. However, most micelle formulations are still in the early stages of development with only one non-cancer related FDA-approved micelle to date.[28]

Promising candidates in overcoming the limitations of other nanocarriers are polymeric nanoparticles as they tend to be more stable than other nanocarriers.[31] Unlike polymeric micelles, most polymeric nanoparticles possess a dense well-defined polymerized core surrounded by a polymeric shell. Furthermore, biodegradable polymeric nanoparticles are highly biocompatible and provide maximum control of the drug release mechanism in response to internal and external stimuli. Unlike other nanocarriers, polymeric nanoparticles enable the precise ratiometric delivery of multiple drugs in high concentrations substantially enhancing the efficacy of single-loaded carriers.[32,33] Drug molecules are typically entrapped in the nanoparticle core or conjugated to the shell effectively preventing premature leakage. A special class of polymeric nanoparticles represent brush-arm star polymers (BASP) containing a densely cross-linked core and a

biocompatible shell. A poly(ethylene)glycol (PEG)-based shell, in particular, represents a well-established method to enhance the blood circulation lifetime of the nanocarrier by preventing renal clearance and aggregation.[34] In addition to cancer therapy, Hung *et. al.* have recently shown the potential of nitroxide-functionalized BASP as metal-free contrast agents that selectively accumulate in tumor tissue.[35]

2.3. Brush-Arm Star Polymers

2.3.1. Synthetic Approaches for the Preparation of Star Polymers

Star polymers represent a class of branched polymers with three-dimensional globular structure typically consisting of linear polymer chains radiating from a central core. Largely driven by the development of controlled living polymerization techniques, star polymers have gained increasing popularity in polymer chemistry as materials with predetermined characteristics and a wide variety of applications.[36] The preparation of star polymers is generally divided into three synthetic approaches: (i) The core-first approach is based on a multifunctional initiator with multiple initiation sites allowing for the simultaneous polymerization of monomers forming the arms of the star polymer (Figure 3a). (ii) The grafting to-approach involves the preparation of end-functionalized polymer arms which selectively couple to a multifunctional linking agent serving as the core (Figure 3b). (iii) In the arm-first approach, a living macroinitiator or macromonomer (arm) is prepared followed by the reaction with a difunctional cross-linker initiating cross-linking reactions between arms radiating from the resulting densely cross-linked core (Figure 3c).
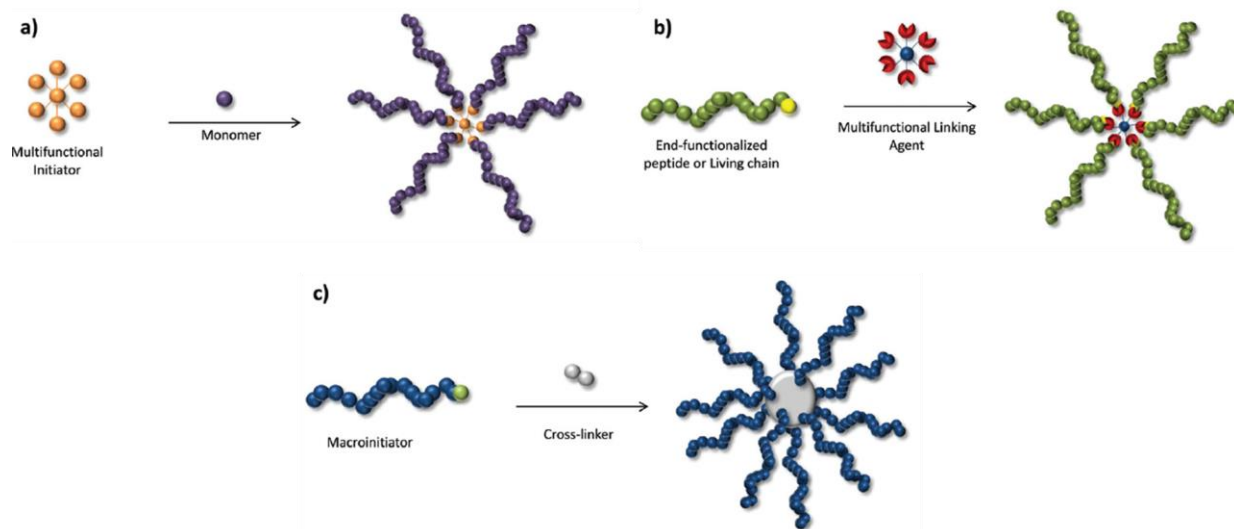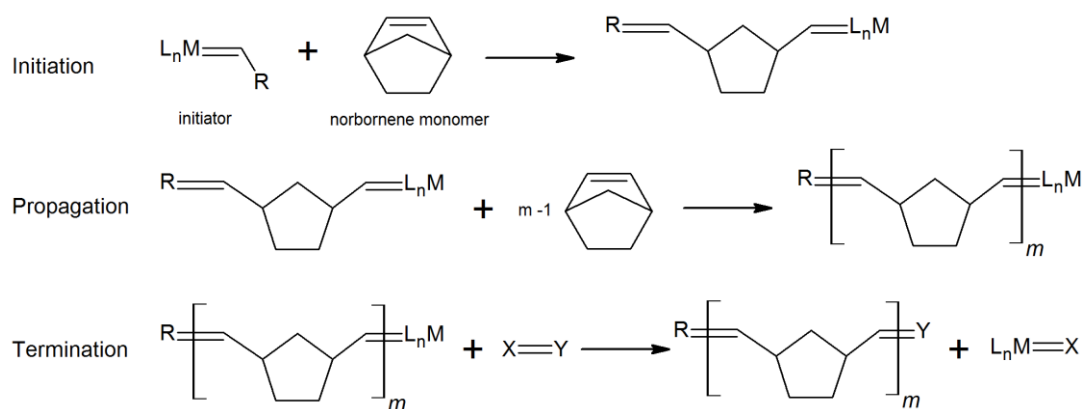
Figure 3. Schematic illustration of strategies for star polymer synthesis with (a) depicting the core-first approach, (b) grafting-to, and (c) arm-first.[37]

Initial attempts to synthesize star polymers were primarily based on the core-first approach due to the high yields and precise control over the number of arms. However, inherent disadvantages such as the difficulty in the characterization of polymer arms, the potential of star-star coupling, and the limited number of arms have shifted the focus to grafting to and arm-first approaches.[38,39] Unlike the core-first approach, grafting to and arm-first strategies allow the direct characterization of polymer arms before core linkage. The grafting to-approach promises the preparation of star polymers with well-defined macromolecular architecture as it allows the precise control over the number of arms per linking agent and chain length. However, steric hindrance around the core typically requires large excess of polymer and long reaction times for adequate conversion while making it difficult to synthesize star polymers with large number of arms.[37] Similar to the graft to-approach, the arm-first strategy enables the preparation of star polymers containing arms with well-defined degree of polymerization. As this method does not require a previously formed core with limited number of initiation sites, star polymers with large number of arms can be produced. Furthermore, the large cross-linked core offers a high capacity for potential

drug-loading making the arm-first approach an attractive method for designing star polymers for cancer treatment.[39]

2.3.2. Polymerization methods

Efforts in synthesizing polymeric nanoparticles rely on highly controllable and efficient polymerization methods with low polydispersity. Previously applied polymerization methods for synthesizing polymeric nanoparticles were mainly based on anionic and radical polymerization, which limits the incorporation of functional moieties (e.g., nitroxides) due to their incompatibility with radical processes.[40,41] Studies by Schrock *et. al.* have laid the foundation for an alternative method, the ring-opening metathesis polymerization (ROMP), by reporting the successful synthesis of star polymers from bis-olefin cross-linkers added to a living polymer chain.[42,43] Additional research by Ogawa and Gutekunst has demonstrated the promise of ROMP as a highly selective method for the one-pot synthesis of star polymers due to its tolerance to most functional groups in therapeutic agents and low dispersity.[44–46] In ROMP involving norbornene monomers, a transition metal initiator reacts with the double bond of norbornene opening up the cyclohexene ring in the initiation step (Figure 4). The two most common transition metal initiators utilized in ROMP are the molybdenum-based Schrock catalyst and the ruthenium-based Grubbs catalysts, which typically shows greater air stability and tolerance for functional groups.[44] As the active initiator is attached to the monomer, chain growth is achieved through further reaction with additional norbornene monomers. The propagation step is terminated by the addition of a linear alkene derivative preventing further chain growth.
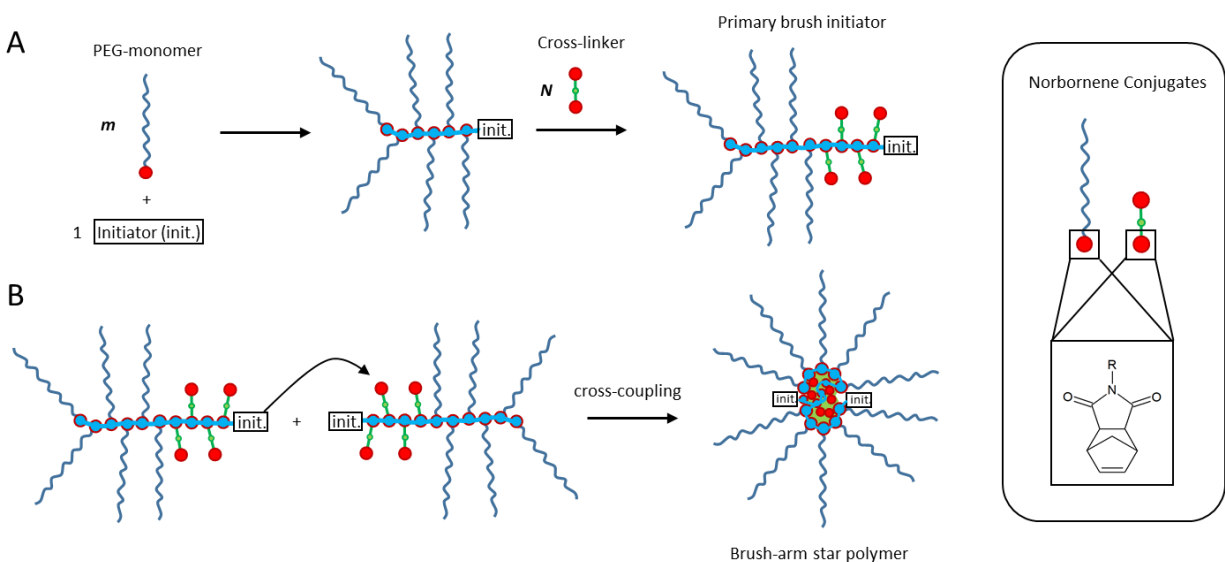
Figure 4. Schematic illustration of initiation, propagation, and termination step in ROMP with generic norbornene monomer and metal initiator. Addition of a linear monomer (XY) terminates polymerization.

2.3.3. Brush-Arm Star Polymer (BASP)

Professor Jeremiah Johnson *et. al*. at Massachusetts Institute of Technology have recently been able to apply ROMP in the context of brush-arm star polymer (BASP).[32,47] As illustrated in Figure 5, BASP contain two functional units: macromonomers (MM) and cross-linkers. The macromonomer, typically a poly(ethylene glycol) (PEG) derivative, determines the physiological solubility and cellular uptake of the BASP nanoparticle.[34] Functionalities such as drug molecules can be built into the macromonomer (graft-through approach) enabling the synthesis of multifunctional BASPs with precise drug ratios. The living brush polymer is formed by ROMP of PEG-macromonomers upon the addition of an initiator in arm-first polymerization, also referred to as brush-first polymerization (Figure 5a). Copolymerization with multifunctional norbornene cross-linkers affords the primary brush initiator with distinct chain length. Subsequent coupling of two primary brush initiators leads to the formation of brush-arm star polymers with a well-defined core stabilized by cross-linking between norbornene cross-linkers, as illustrated in Figure 5b. As the core still contains active initiators and unreacted norbornene groups, further star growth can occur via the bimolecular coupling of star polymers at longer time scales. Alternatively, the addition of extra equivalences of MM results in further polymerization (ROMP-out) forming a

denser shell. Termination of star growth and ROMP-out is achieved through the addition of a linear monomer or steric interactions.[47]

Figure 5. Schematic illustration of brush-arm star polymer formation steps: (A) primary brush initiator formation upon ROMP of PEG-macromonomer and addition of crosslinker, and (B) star formation upon cross-coupling of two brush polymers. Relative equivalences of PEG-macromonomor and cross-linker are labeled as *m* and *N*, respectively. Adapted from Liu, J.; Burts, A. O.; Li, Y.; Zhukhovitskiy, A. V.; Ottaviani, M. F.; Turro, N. J.; Johnson, J. A. *J. Am. Chem. Soc.* 2012, *134* (39), 16339.

The diameter and molecular weight of the resulting BASP can be controlled by varying *N*, the degree of polymerization of cross-linker. Furthermore, Liu *et. al.* demonstrated the effect of increasing *N* on the polydispersity, as illustrated in Figure 6a. Multiple mass distributions were observed for BASP with equal equivalents of cross-linker to MM, whereas increasing the ratio of cross-linker to MM yielded nanoparticles with low PDI and larger molecular weight. A statistically significant positive logarithmic relationship was obtained between *N* and the molecular weight suggesting increased cross-linking and core size (Figure 6a, b).[47] In particular, increasing *N* by 5 resulted in a doubling of the BASP molecular weight. The opposite trend is observed for varying *m*, the degree of polymerization of the macromonomer. At constant *N*, an increase in *m* decreases the molecular weight due to steric hindrance during cross-linking. Thus, resulting BASP will be smaller in size as further dimerization events are suppressed.
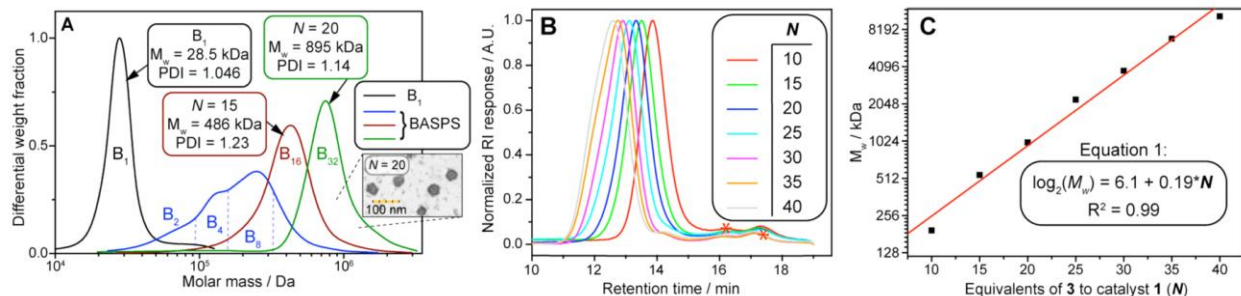
Figure 6. (A) Differential mass GPC traces for BASPs with N = 10, 15, and 20 after 4 h cross-linking. (B) Refractive index GPC traces of N = 10–40 BASP where red asterisks indicate unreacted MM and brush polymer. (C) Log$_2$ plot of M_w versus N corresponding to BASP series from (B). Reproduced from Liu, J.; Burts, A. O.; Li, Y.; Zhukhovitskiy, A. V.; Ottaviani, M. F.; Turro, N. J.; Johnson, J. A. *J. Am. Chem. Soc.* 2012, *134* (39), 16337–16344.

2.3.4. BASP Core Degradation and Drug Release

As the main molecule involved in core formation during BASP synthesis, the choice of cross-linker provides a powerful tool in modifying the core stability of the particle with respect to stimuli-responsive core degradation. Cross-linkers used in ROMP-based BASP synthesis typically consist of a bis-norbornene linked by a variable linker part. Cleavage of this linker in BASP promises an attractive target for core degradation resulting in regeneration of parent brush polymers facilitating drug release and efficient in vivo clearance. To date, several different types of cross-linkers that cleave in response to pH, light, and reduction potential have been proposed and tested.[32,48,49] Acid-labile acetal-based cross-linkers, in particular, have shown promising results in enabling BASP degradation under highly acidic conditions.[49] However, rapid core degradation triggered by slightly acidic pH necessary for selective drug release in tumor tissue remains a formidable challenge.

As BASP degradation initiated by the cleavage of cross-linker does not affect the linkage between MM and prodrug, drug release is achieved in a separate mechanistic step enabling specific individual trigger for core degradation and drug release (Figure 7). A well-established method of drug release that has recently been applied in the context of PEG-based BASP is the enzymatic hydrolysis of the MM-prodrug linkage followed by 1,6 elimination.[33] These types of linker

typically consist of amine-containing carbamates or carbonates providing predictable rates of drug release.[50] Other linkers commonly used in research include photocleavable nitrobenzene-functionalized tether that trigger drug release in response to ultraviolet light.[51]
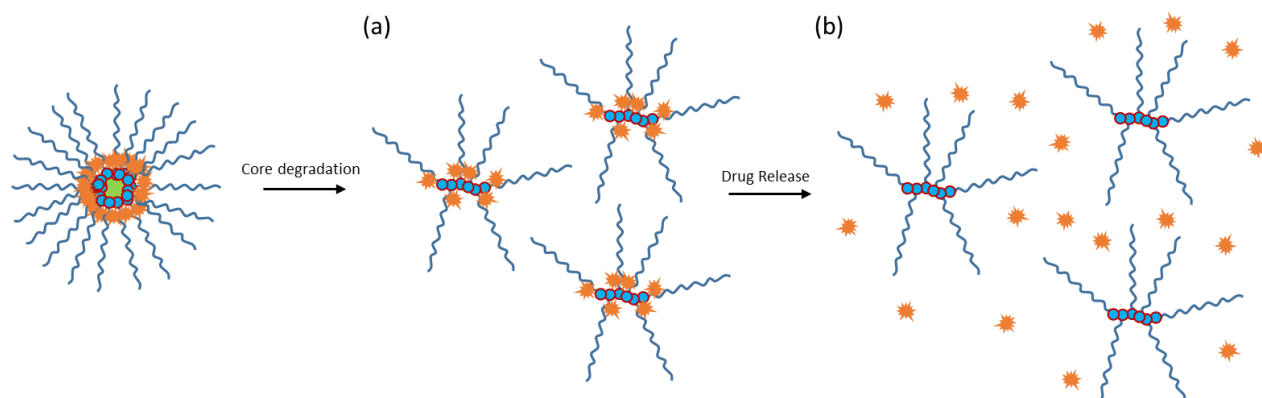
Figure 7. Schematic illustration of BASP core degradation followed by drug release. Orange stars represent a generic drug molecule.

2.3.5. BASP in Cancer Treatment

While research on single-drug-loaded nanoparticles has led to several FDA-approved nanoparticle-based formulations with improved efficacy of chemotherapy, certain cancer types may require the combination of multiple drugs for effective treatment.[52] Thus, a nanocarrier that enables the administration of multiple drugs with different biological targets and cytotoxic profiles promises even more effective forms of cancer therapy. BASPs provide the optimal platform for a targeted multi-drug delivery with maximum control of drug release kinetics. The graft-through approach allows the precise tuning and efficient synthesis of nanoparticles with varying drug-loading ratios for cancer-specific formulations.

Researchers at Massachusetts Institute of Technology have recently demonstrated the synthesis of multidrug-conjugated BASP for the ratiometric delivery and synchronized drug release near their respective MTD.[32] BASPs used in their study contained MMs conjugated with camptothecin and doxorubicin, as well as a cisplatin-based cross-linker representing the first

successful work on triplex drug delivery according to the authors. Core degradation of BASP was achieved by reduction of labile Pt-O bonds in the cross-linker resulting in rapid release of cytotoxic cisplatin. Subsequent drug release of camptothecin and doxorubicin from regenerated brush polymers occurred via enzymatic hydrolysis and photocleavage, respectively.

Additional studies investigated the therapeutic tolerance and efficacy of this BASP compared to its analogous free drug formulation in treating certain types of xenograft tumors in mice.[33] RNAi signature assay confirmed that the subcellular mechanism of action of BASP-bound drugs is equivalent to that of the corresponding free drug resulting in inhibition of cell growth or apoptosis. Figure 8a demonstrated the passive accumulation of BASP in the tumor via EPR effect enabled by a blood circulation half-time of 3.2 h. Comparison of the average body mass indicated consistent body masses for BASP-treated and control mice, whereas mice treated with the free drug formulation significantly lost body mass before being euthanized after 10 days (Figure 8b). The efficacy of BASP treatment was evaluated by monitoring the tumor volume progression, as illustrated in Figure 8c. BASP-treated mice showed a regression in tumor growth compared to the control group along with an enhanced survival rate (Figure 8c).
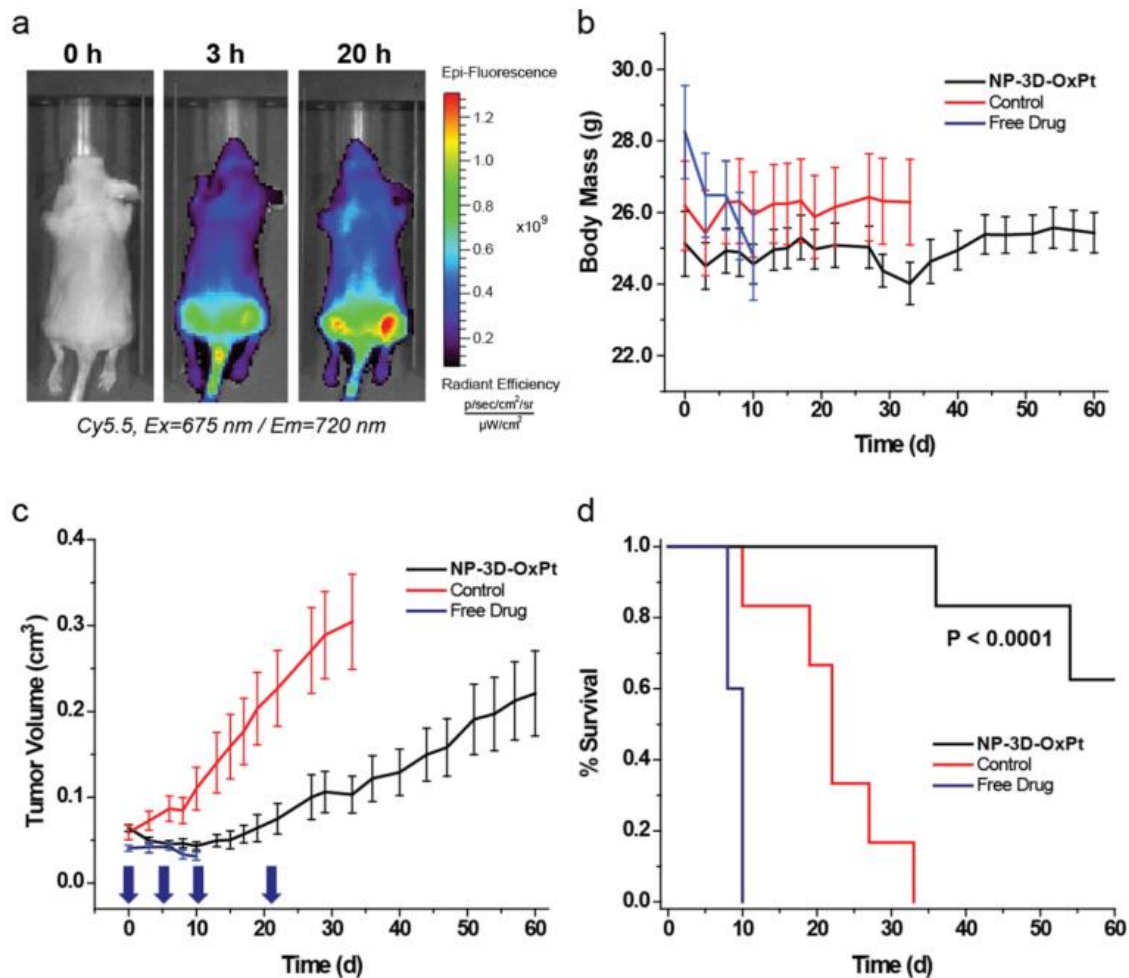
Figure 8. Therapeutic tolerance and efficacy studies of three-drug-conjugated BASP containing cisplatin, camptothecin, and doxorubicin.[33] (a) shows the localization of BASP in two subcutaneous SKOV-3 xenograft tumors in a NCR-NU mouse observed 20 h after injection via epi-fluorescence with excitation and emission wavelengths of Cy5.5 fluorophore of 675 nm and 720 nm, respectively. (b) Average body mass and (c) average tumor volume progression of mice treated with BASP, control, and free drug formulation (blue arrows indicate injections on days 0, 5, 11, and 22). The survival rate of the three groups was assessed via Kaplan-Meier survival curve (d).

While these studies have demonstrated the potential of multidrug-conjugated BASP in improving the efficacy of conventional chemotherapy, recent efforts focus on further increasing the drug-loading per particle by structural diversification. Modifying the BASP core with hydrophilic components to form a star-like nanogel may improve the drug release by enhancing the diffusion of hydrophobic drugs out of the core as well as leading to a more rapid core degradation. Furthermore, star-like nanogels have shown to further increase drug-loading levels by

providing swelling properties.[53] In this thesis, we will investigate structural modification methods to expand the BASP core and increase drug-loading.

2.4. Methodologies

2.4.1. Gel Permeation Chromatography (GPC)

As a type of size-exclusion chromatography, gel permeation chromatography (GPC) represents the standard methodology for the molecular characterization of branched and unbranched polymers. First introduced by Moore in 1964, GPC separates a mixture of polymers based on their hydrodynamic volume.[54] Following the general procedure, the analyte mixture is dissolved in GPC solvent and injected into the instrument. The flow of additional solvent forces the injected mixture through a column containing microporous gel beads with size-dependent affinity for analytes, as illustrated in Figure 9. Smaller analytes readily enter the pores and are retained by the stationary phase, whereas larger analytes are partially excluded by the smaller pore sizes remaining in the mobile phase. As a result, larger analytes migrate faster through the column and elute earlier than smaller analytes.

The elution of analytes is continuously monitored by detectors categorized by their detection method. Concentration-sensitive detectors based on differential refractive index (DRI), UV/visible absorption, and IR absorption measure the concentration of analyte in the eluent to calculate molar mass averages and distributions.[55] Furthermore, static light scattering detectors such as low- and multi-angle light scattering (LALS and MALS) provide additional information about the molar mass and size as well as aggregation effects of the analyte.[56] In the context of BASPs, the shape and width of the analyte peaks obtained by these methods enable the detailed analysis of polydispersity and BASP composition.
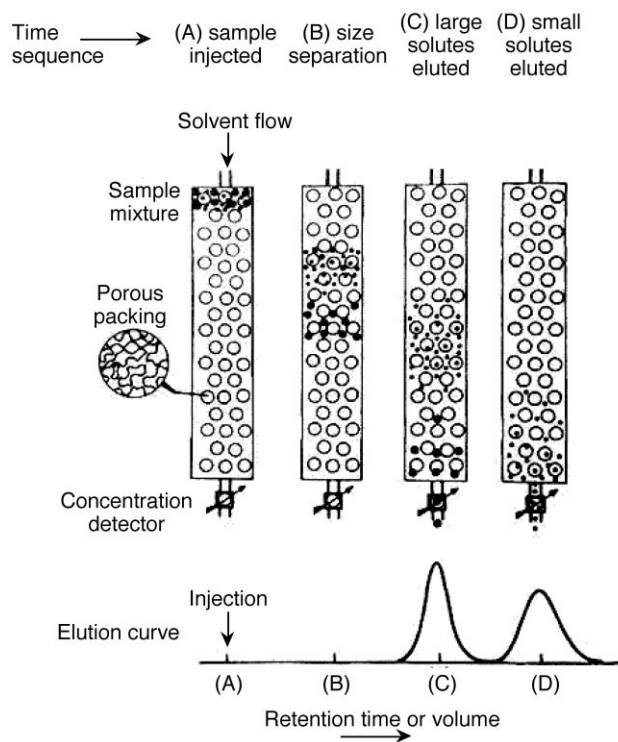
Figure 9. Schematic illustration depicting the basic principle of gel permeation chromatography.[55]

2.4.2. Fluorescence Spectroscopy

Fluorescence spectroscopy is a highly sensitive analytical tool for the quantitative measurement of fluorescence emission from a sample.[57] Fluorescence is based on the radiative transition from an excited electronic singlet state to the ground state in a molecule referred to as fluorophore. As the fluorescence intensity in dilute samples is proportional to the concentration of the fluorophore, fluorometry enables the accurate determination of fluorophore concentration in a sample.[58] Fluorophores with distinct excitation and emission wavelengths are typically used to label non-fluorescent analytes in efforts to relate fluorescence intensity to analyte concentration. Furthermore, special classes of fluorophores such as fluorescein dye can mimic the affinity of hydrophobic drug molecules to nanocarriers correlated to the fluorescence intensity of the nanocarrier-fluorophore complex.

2.5. Objectives

The overall goal of this work is to improve the architecture of the BASP-platform in efforts to enhance the drug-loading and core-degradability in response to acidic environment. In particular, this thesis seeks to accomplish the following objectives:

1. Synthesize acid-labile star-like nanogels containing acetal cross-linker and PEG-macromonomer via brush-first ROMP

2. Investigate the effect of varying the ratio of cross-linker to PEG-macromonomer on core formation and nanogel size

3. Study the diffusion of a hydrophobic fluorescent molecule in and out the nanogel core

4. Investigate the core degradation of the nanogel in response to acidic pH

Star-like nanogels synthesized by simultaneous addition of cross-linker and PEG-MM during core formation are hypothesized to have a significantly larger core size and molecular weight compared to regular BASP. Furthermore, the copolymerization with PEG-MM is expected to decrease the extent of cross-linking resulting in a more hydrophilic, gel-like BASP core. As a result, the diffusion of molecules in and out the core as well as feasibility of core degradation in acidic pH are predicted to improve with the proposed structural changes.

3. Methods

All reagents and solvents were purchased from commercial suppliers and used as received unless otherwise noted. Nuclear magnetic resonance (NMR) spectra were recorded on a JEOL Eclipse 300 MHz NMR spectrometer and a Bruker AVANCE-400 NMR spectrometer. Gel permeation chromatography (GPC) analyses of BASP were performed at Massachusetts Institute of Technology (MIT) on an Agilent 1260 Infinity setup with two Shodex KD-806M columns in tandem and a 0.025 M LiBr DMF mobile phase run at 60 °C. BASP samples for GPC were diluted in 0.025 M LiBr DMF and filtered through a 0.45 µm PTFE filter. Acid-degraded samples were prepared by adding a drop of concentrated trifluoroacetic acid (TFA) to the BASP nanogel solution in dichloromethane. After 24 hours the solvent was removed by vacuum and samples reimmersed in 0.025 M LiBr DMF before performing GPC measurements. A Wyatt Optilab T-rEX detector was used to monitor the differential refractive index (dRI) and the light scattering (LS) signal was acquired with a Wyatt Dawn Heleos-II detector. The fluorescence intensity of BASP samples containing fluorescein dye were performed on a Photon Technology International QuantaMaster 8000 Fluorimeter.

### 3.1. Fluorescein Loading of BASP Nanogels

The equivalent volume of 5 mg BASP nanogel sample was added to 2 mL of 1 µM fluorescein sodium salt in nanopure water. After 24 hours, the solution was dialyzed against 500 mL nanopure water for 1 d using regenerated cellulose dialysis tubing (Spectrum Labs, 8 kDa MWCO). The solvent was removed by vacuum and the resulting solid reimmersed into 2 mL nanopure water via sonication for 30s. Samples for fluorescence measurements were prepared by filling the cuvette with 3 mL of nanopure water followed by the addition of 0.2 mL fluorescein

loaded sample solution. Fluorescence intensities were obtained using an excitation wavelength of 490 nm with all slits set to 1 nm.

3.2. Fluorescein Dye Release

A cuvette was filled to the top with nanopure water and the cuvette cap with a dialysis membrane wrapped around (Spectrum Labs, 8 kDa MWCO) placed on top. After a constant fluorescence reading was obtained at an emission wavelength of 510 nm (excitation wavelength 438 nm, all slits set to 2 nm), 200 µL of fluorescein loaded BASP nanogel sample was added through a hole to the cuvette cap. Core degradation was initiated 60 min later through the addition of 23 µL of 1 M trifluoroacetic acid to the cuvette cap lowering the pH of the solution to 2.

3.1. Synthesis of Norbornene-Poly(ethylene glycol) (PEG) Macromonomer
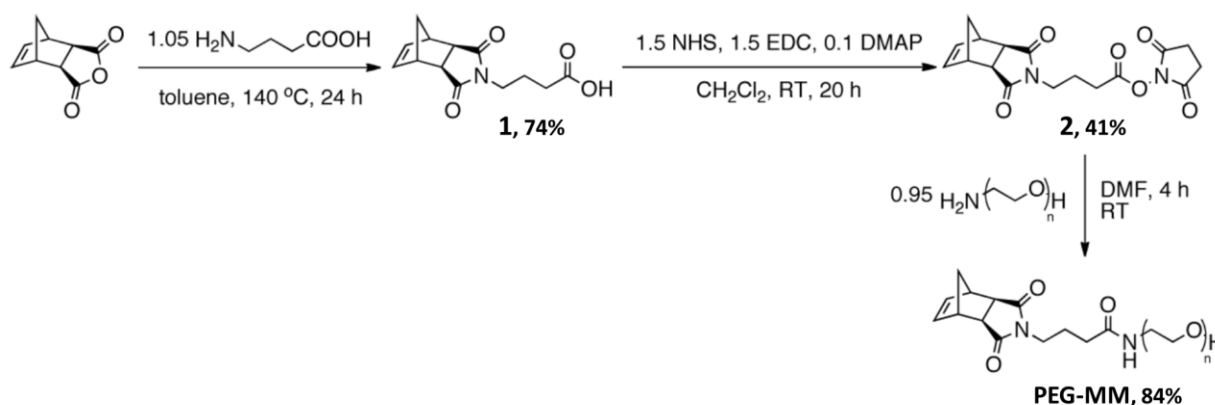
Figure 10. Synthesis of norbornene-poly(ethylene glycol) macromonomer (**PEG-MM**) from gamma-aminobutyric acid, cis-5-norbornene-exo-2,3-dicarboxylic anhydride, N-Hydroxysuccinimide, and *O*-(2-Aminoethyl)poly(ethylene glycol).[47]

3.1.1. Norbornene-Butyric Acid 1

A solution of gamma-aminobutyric acid (1.65 g, 16.00 mmol) and cis-5-norbornene-exo-2,3-dicarboxylic anhydride (2.50 g, 15.20 mmol) in toluene (75 mL) was stirred at 140 °C in an oil bath under reflux for 24 h. The resulting product mixture was purified by washing with 1M HCl

(3x, 75 mL) and brine followed by drying over anhydrous MgSO4 MgSO₄. Solvent was removed *in vacuo* to afford **1** (2.798 g, 74% yield) as a faint white solid. ^{1}H NMR (300 MHz, CDCl₃): δ 6.28 (s, 2H), 3.54 (t, 2H), 3.27 (s, 2H), 2.69 (d, 2H), 2.37 (t, 2H), 1.93 – 1.86 (m, 2H), 1.52 (d, 1H), 1.20 (d, 1H).

3.1.2. Norbornene-N-Hydroxysuccinimidyl (NHS)-Ester 2

N-Hydroxysuccinimide (NHS, 1.94 g, 16.90 mmol), 4- (dimethylamino)pyridine (DMAP, 137 mg, 1.10 mmol) and **1** (2.79 g, 11.20 mmol) were completely dissolved in dichloromethane (115 mL) before addition of N-(3-dimethylaminopropyl)-N'-ethylcarbodiimide hydrochloride (EDC, 2.80 g, 16.90 mmol). After stirring the solution at room temperature for 20 h, the resulting reaction mixture was concentrated by rotary evaporation and purified via silica gel column chromatography (70% EtOAc/hexanes) to obtain **2** (2.416 g, 41% yield) as a white solid. ^{1}H NMR (300 MHz, CDCl₃): δ 6.29 (s, 2H), 3.59 (t, 2H), 3.28 (s, 2H), 2.83 (s, 4H), 2.71 (d, 2H), 2.65 (t, 2H), 2.05 – 1.98 (m, 2H), 1.53 (d, 1H), 1.19 (d, 1H).

3.1.3. Norbornene-PEG Macromonomer

O-(2-Aminoethyl)poly(ethylene glycol) (1.00 g, 0.33 mmol) and **2** (0.12 g, 0.35 mmol) were dissolved in 13 mL anhydrous dimethylformamide and stirred at room temperature for 24 h. Precipitation in diethyl ether (200 mL) followed by vacuum filtration and washing with two equivalents of diethyl ether yielded **PEG-MM** (0.930 g, 84% yield) as a white solid. ^{1}H NMR (300 MHz, CDCl₃): δ 6.43 (s, 1H), 6.28 (t, 2H), 3.87 (t, 2H), 3.82 – 3.32 (m, 363H), 3.26 (t, 3H), 2.78 (s, 1H), 2.68 (d, 2H), 2.16 (t, 5H), 1.94 – 1.87 (m, 2H), 1.78 (m, 20H), 1.52 (d, 1H), 1.20 (d, 1H).

3.2. Synthesis of Acetal Cross-Linker
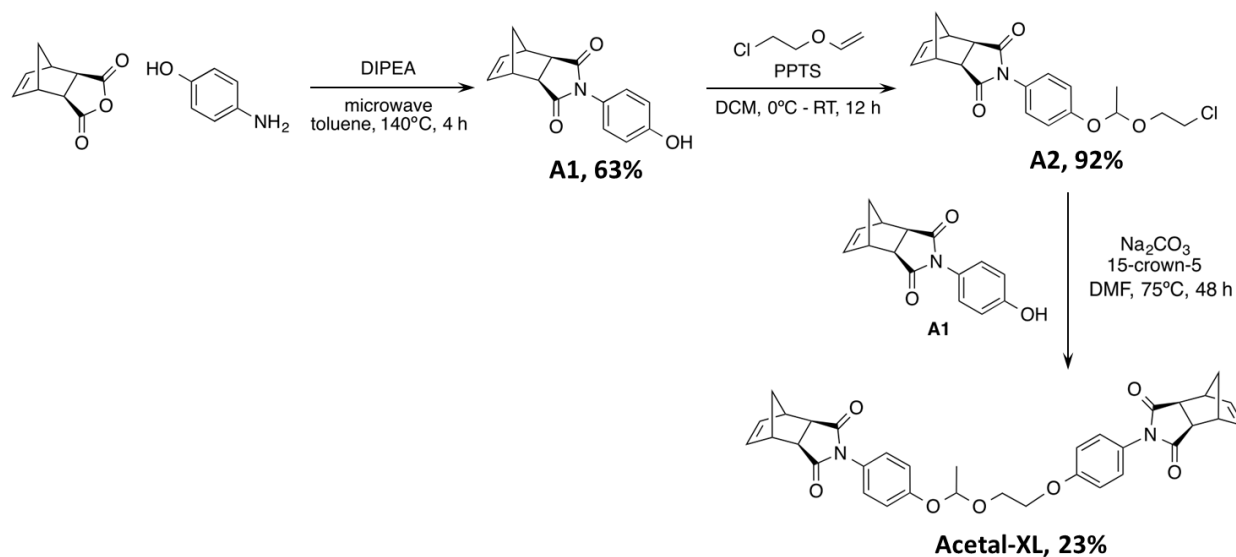
Figure 11. Synthesis of acetal cross-linker (**Acetal-XL**) from cis-5-norbornene-exo-2,3-dicarboxylic anhydride, 4-aminophenol, and 2-chloroethyl vinyl ether.[49]

3.2.1. Compound A1

A mixture of cis-5-norbornene-exo-2,3-dicarboxylic anhydride (1.175 g, 7.15 mmol), 4-aminophenol (1.013 g, 9.28 mmol), and N,N-diisopropylethylamine (1.62 mL, 9.28 mmol) in toluene (17 mL) was heated at 140 °C for 4 h. After concentration via rotary evaporation, the solution was re-dissolved in hot methanol (20 mL) followed by filtration. Cooling the filtrate to 0 °C resulted in white crystals which were filtered and recrystallized twice in methanol to afford **A1** (1.133 g, 63% yield). ^{1}H NMR (400 MHz, DMSO-d6) δ 9.73 (s, 1H), 7.04-7.00 (m, 2H), 6.84-6.81 (m, 2H), 6.36-6.35 (m, 2H), 3.19-3.18 (m, 2H), 2.80 (s, 2H), 1.47-1.44 (m, 1H), 1.38 (d, 1H).

3.2.2. Compound A2

Pyridinium p-toluenesulfonate (0.061 g, 0.241 mmol) and **A1** (0.616 g, 2.41 mmol) were dissolved in dichloromethane (60 mL) and cooled down to 0°C in an ice bath followed by dropwise addition of 2-chloroethyl vinyl ether (1.22 mL, 12.0 mmol). After stirring for 12 h under nitrogen

atmosphere, the solution was washed with saturated sodium bicarbonate, water, and brine. Drying over sodium sulfate followed by silica gel chromatography (0%-30% EtOAc/hexanes) yielded **A2** (0.804 g, 92% yield). ^{1}H NMR (400 MHz, CDCl$_3$) δ 7.16-7.12 (m, 2H), 7.08-7.04 (m, 2H), 6.30 (t, 2H), 5.45 (q, 1H), 3.92-3.86 (m, 1H), 3.75-3.69 (m, 1H), 3.58-3.54 (m, 2H), 3.35 (s, 2H), 2.79 (s, 2H), 1.57 (d, 1H), 1.42 (d, 1H).

3.2.3. Acetal Cross-Linker

A2, **A1**, Na$_2$CO$_3$, and 15-crown-5 were dissolved in dimethylformamide (15 mL) and stirred at 75 °C for 48 h under nitrogen atmosphere. After dilution with ethyl acetate, the reaction mixture was washed with saturated sodium bicarbonate, water, and brine followed by drying over sodium sulfate. Purification of the crude product by silica gel chromatography (0%-50% EtOAc/hexanes) afforded **Acetal XL** cross-linker (0.241 g, 23% yield). ^{1}H NMR (400 MHz, CDCl$_3$) δ7.16- 7.08 (m, 6H), 6.92-6.90 (m, 2H), 6.32 (m, 4H), 5.51 (q, 1H), 4.10-4.08 (m, 2H), 4.02- 3.97 (m, 1H), 3.88-3.83 (m, 1H), 3.38-3.37 (m, 4H), 2.81 (d, 4H), 1.59 (dqt, 2H), 1.55 (d, 3H), 1.45 (d, 2H).

3.3. Synthesis of Brush-Arm Star Polymer Nanogels

In a glove box under nitrogen atmosphere**, PEG-MM** (0.010 g, 0.0031 mmol) was dissolved in anhydrous 1,4-dioxane (48.0 µL) and freshly prepared Grubbs 3rd generation catalyst added (0.02 g/mL dioxane, PEG-MM:catalyst = 10) to give a total **PEG-MM** concentration of 0.05 M. After 20 min stirring at room temperature, a mixture containing the desired equivalents of **acetal XL** cross-linker and **PEG-MM** was prepared from **Acetal XL** (0.1 M) and **PEG-MM** (0.05 M) stock solutions and added to the reaction mixture. The reaction was quenched with ethyl vinyl ether (20 µL) after additional 100 min of stirring.

4. Results and Discussion

4.1. Synthesis of BASP Nanogels

BASP nanogels were synthesized via brush-first ROMP involving the homopolymerization of 10 equivalences of norbornene-functionalized PEG-MM initiated by one equivalence of Grubbs 3rd generation initiator (Figure 12). After the formation of the living bottle-brush polymer a mixture of PEG-MM and acid-cleavable acetal cross-linker was added to induce core formation and cross-linking. The ratio of acetal XL (N) to PEG-MM (m) was varied between 10 to 30 equivalences of acetal XL and 0 to 20 equivalences of PEG-MM in order to investigate the effect on the BASP nanogel structure.
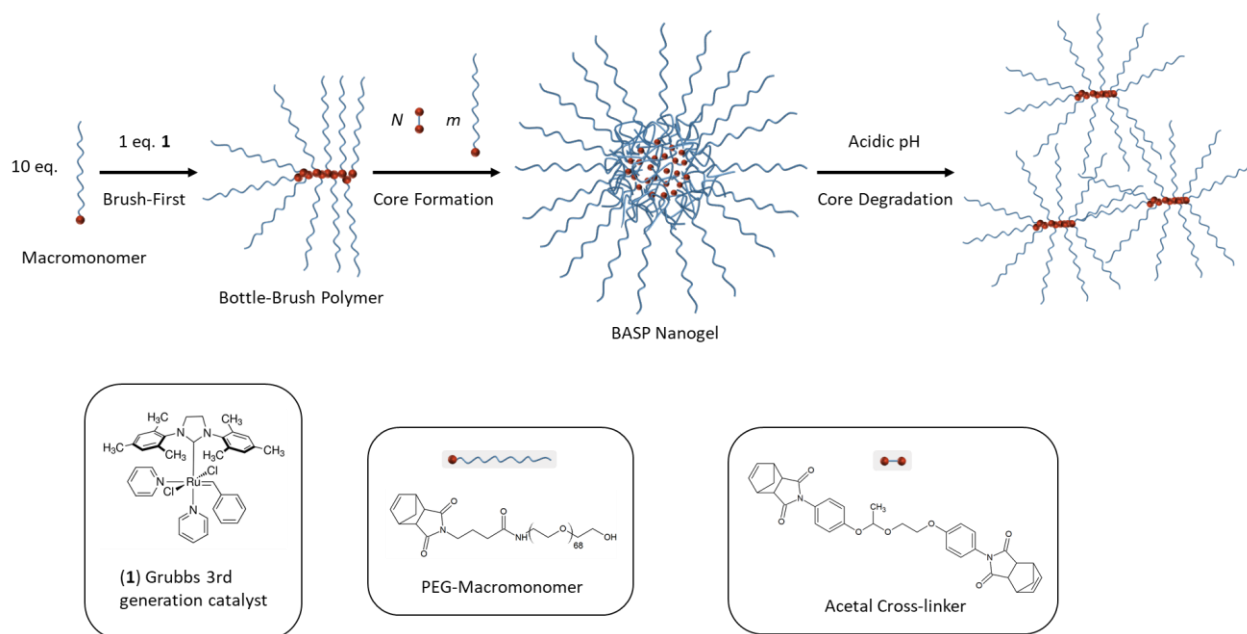

Figure 12. Synthesis of poly(ethylene glycol) BASP nanogel via brush-first ring-opening metathesis polymerization followed by acid-triggered core degradation.

4.2. Gel Permeation Chromatography Studies

The synthesized BASP nanogels were analyzed for their size and dispersity via GPC. Figure 13 shows the GPC traces obtained for BASP nanogel samples with N = 10 and m = 0, 5, 10, and

Grundler 28

20. The BASP nanogel sample where no PEG-MM was added during cross-linking resulted in a well-defined peak with the shortest retention time followed by BASP nanogels with m = 20, m = 10, and m = 5. The peaks for BASP nanogels with m = 5 and m = 20 show an almost identical retention time with the m = 5 sample eluting out slightly earlier. Notably, the m = 5 peak is significantly broader than m = 0 and m = 20 peaks suggesting multiple mass distributions. The longest retention time is observed for the m = 10 BASP nanogel corresponding to the lowest MW. This data indicates that the addition of PEG-MM during cross-linking decreases the MW of the resulting BASP nanogel.
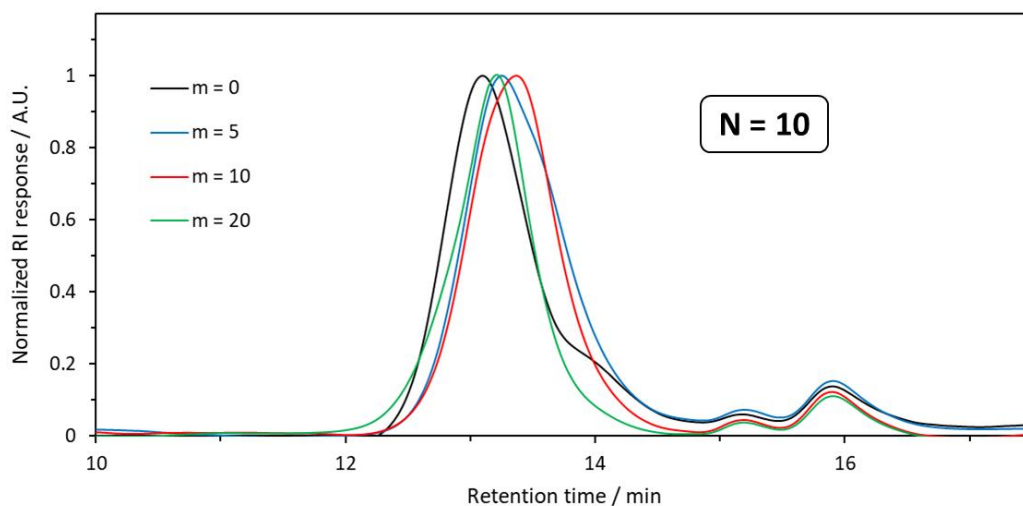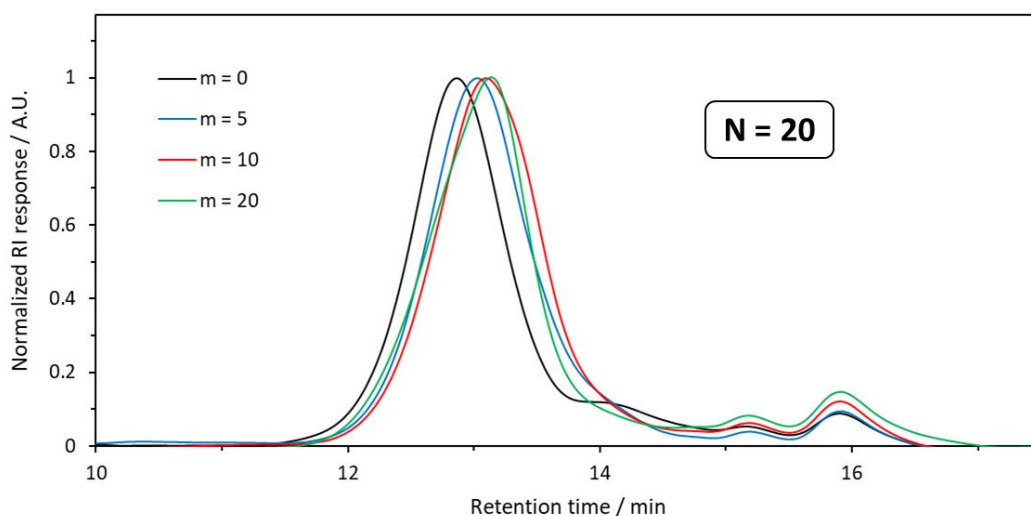

Figure 13. Refractive index GPC traces of N = 10 BASP nanogels showing the effect of varying the amount of PEG-MM added during cross-linking.

A similar trend is observed for BASP nanogels with N = 20 (Figure 14) and N = 30 (Figure 15). In both cases, the m = 0 BASP nanogel exhibits a significantly shorter retention time than corresponding BASP nanogels with additional PEG-MM added. However, unlike BASP nanogels with N = 10, the m = 20 BASP nanogel has the longest retention time followed by m = 10 and m = 5. Generally, the peaks observed in GPC become broader as more PEG-MM is added suggesting an increasing polydispersity. In particular, the peak for the N = 30, m = 20 BASP nanogel is

significantly broader than the peaks for BASP nanogels containing less PEG-MM. However, the well-defined Gaussian peak shape suggests a mostly monomodal MW distribution for all N and m tested with the exception of m = 0 BASP nanogels.

The shoulder peak observed around 14 min indicates the presence of a second species with a MW slightly smaller than that of the corresponding cross-linked BASP nanogel. A similar phenomenon was previously reported by Gao et al. who identified the shoulder peak of a N = 15 BASP with acetal XL as unconverted bottle-brush polymer.[49] The shoulder becomes less defined as m increases indicating increasing conversion of bottle-brush polymer to BASP. Only N = 30 BASPs GPC traces show a shoulder regardless of the equivalences of PEG-MM added.

Figure 14. Refractive index GPC traces of N = 20 BASP nanogels showing the effect of varying the amount of PEG-MM added during cross-linking.
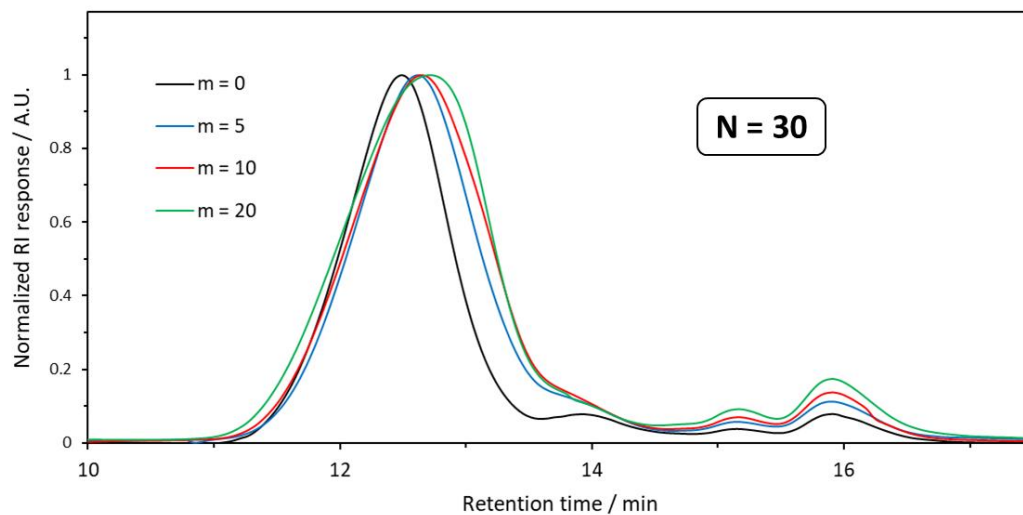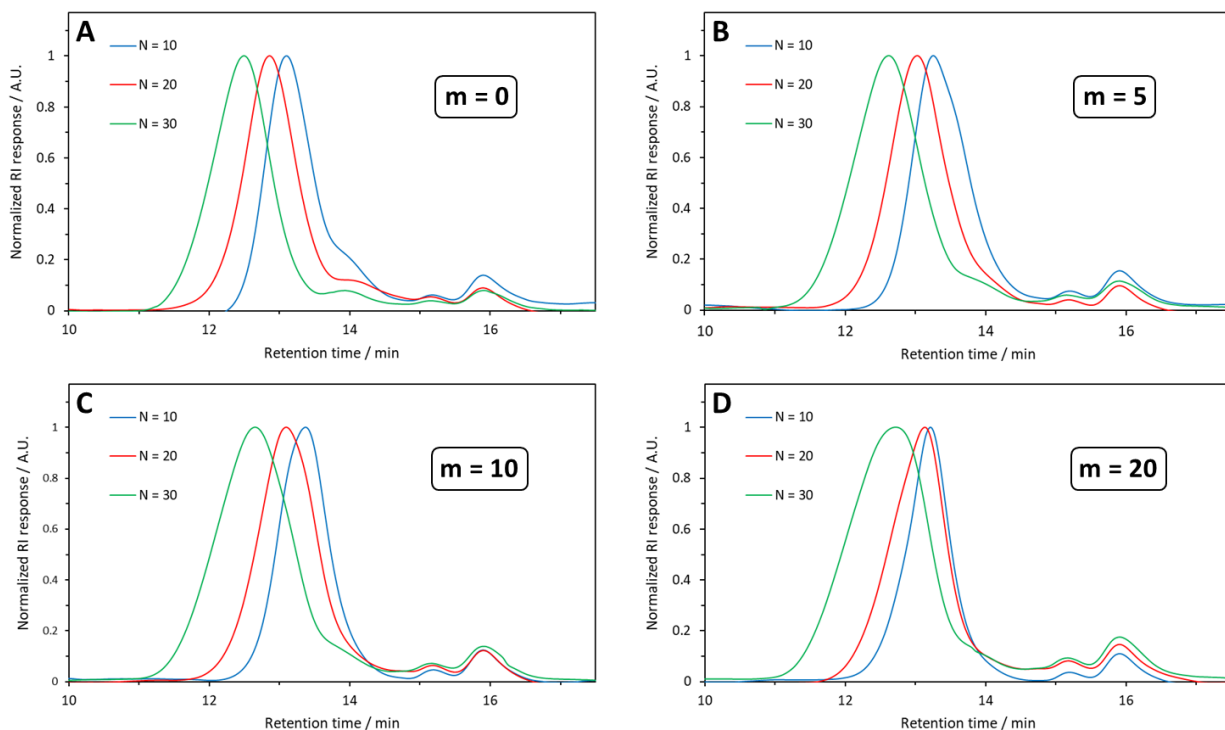
Figure 15. Refractive index GPC traces of N = 30 BASP nanogels showing the effect of varying the amount of PEG-MM added during cross-linking.

Direct comparison of GPC traces obtained for regular BASP without the addition of PEG-MM during cross-linking is shown in Figure 16a. The N = 10 BASP resulted in the shortest retention time followed by N = 20 and N = 30 indicating an increasing MW as the equivalence of acetal XL is increased. These results agree with a previous study by Liu et al. who tested the effect of varying the ratio of a nitrobenzyloxycarbonyl bis-norbornene cross-linker on the MW of the resulting BASP.[47] The authors found a positive logarithmic relationship between the amount of cross-linker and the BASP MW based on the increased cross-coupling of bottle-brush polymers.

As previously mentioned, a shoulder around 14 min is observed in the GPC traces of m = 0 BASPs corresponding to unconverted bottle-brush polymer. The shoulder height decreases as N increases indicating higher conversion of bottle-brush polymer to BASP via cross-coupling. The increasing efficiency of the cross-coupling step is theorized to be based on the combined effect of the increasing number of available cross-linking sites as well as the reduced steric hindrance due to the increased amount of cross-linker and larger core size. This trend is also evident in Figure 16b and c showing the GPC traces of m = 5 and m = 10 BASP nanogels, respectively. However,

as m is increased to 20, peaks corresponding to N = 10 and N = 20 BASP nanogel almost overlap indicating a similar MW despite the different amounts of cross-linker added (Figure 16d). Notably, the peaks for N = 10 and N = 20 BASP maintain their narrow shape suggesting well-defined monomodal BASP nanogels regardless of m. In contrast, N = 30 BASP nanogel peaks become significantly broader as m increases correlating to a broader MW distribution.

Figure 16. Refractive index GPC traces of BASP nanogels with (a) m = 0, (b) m = 5, (c) m = 10, and (d) m = 20 showing the effect of varying the amount of cross-linker on the retention time.

These observations raise questions about the structure of the resulting BASP nanogels as well as their growth mechanism. Unlike hypothesized, the simultaneous addition of macromonomer and cross-linker during core formation does not increase the MW and size of the BASP nanogel. The significant shift in retention time between regular m = 0 BASP and m = 5, 10, 20 BASP nanogels suggests that the addition of the macromonomer negatively affects the core formation step. In fact, the heteropolymerization of macromonomer and cross-linker is expected to

increase the steric hindrance preventing access to the bottle-brush initiator as shown in the proposed mechanism in Figure 17. As a result, available cross-linking sites become less accessible as the macromonomer prevents the interaction with other bottle-brush initiators decreasing the probability of successful cross-coupling reactions (i.e., formation of BASP nanogel).

While it is unclear how much PEG-MM was incorporated into the BASP core, the obtained results suggest a saturation level of PEG-MM incorporation based on the ratio of PEG-MM to cross-linker (m:N). In particular, the Johnson group has found that ROMP of a structurally related bis-norbornene cross-linker is substantially faster compared to PEG-MM, implying only a limited incorporation of PEG-MM before cross-coupling occurs.[47] This agrees with the observation that the MW slightly decreases as m increases from 5 to 10 for N = 10 BASP nanogels as indicated by Figure 13. However, the increase in MW for the m = 20 BASP nanogel suggests an additional mechanistic step. After cross-coupling and core formation, the BASP nanogel still contains living initiator that can react with macromonomer that had not been previously incorporated into the BASP nanogel core in a step referred to as ROMP-out (Figure 17). As a result, the MW and size of the resulting BASP nanogel becomes larger compared to m = 5 and m = 10 BASP nanogels.

This effect is less evident in N = 20 and N = 30 BASP nanogels as a larger amount of cross-linker allows the incorporation of more PEG-MM in the cross-coupling step as opposed to after the core is formed (i.e., ROMP-out cannot occur). Furthermore, the increasing broadness of the N = 30 BASP nanogel peak as m increases provides evidence for this theory as the incorporation of more PEG-MM will ultimately increases the number of statistical combinations during cross-coupling and therefore the polydispersity of the sample (Figure 15).
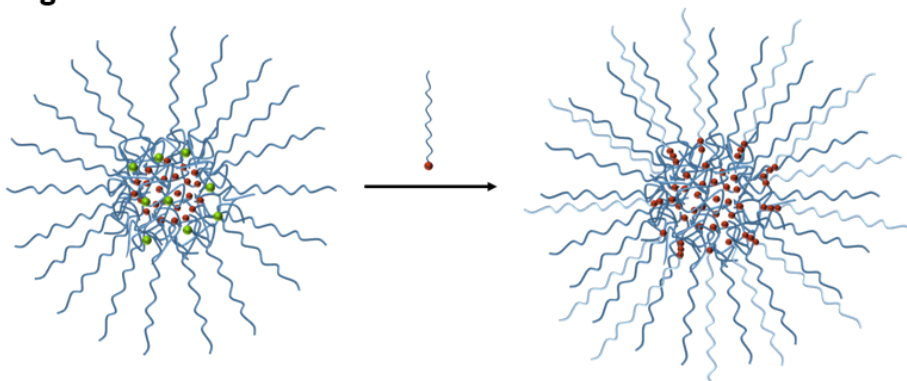
Stage I: ROMP-in (Chain-growth of bottle-brush initiator)
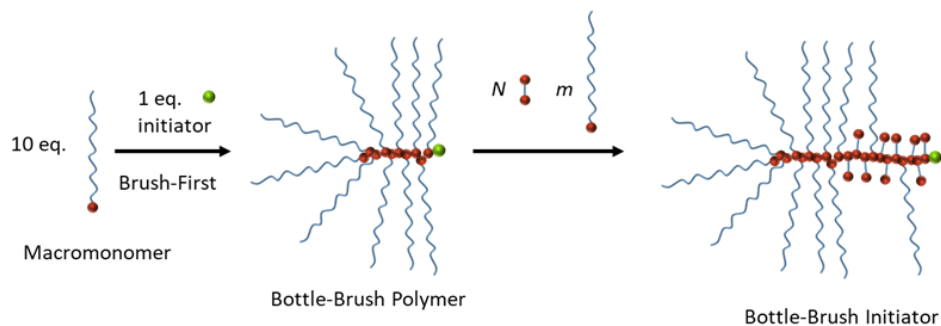
## Stage II: Cross-coupling and core formation
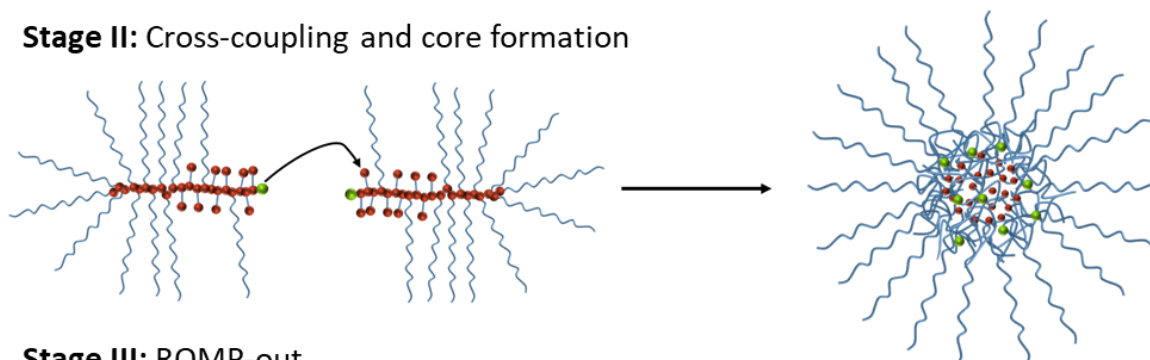
Stage III: ROMP-out

Figure 17. Proposed mechanism of BASP nanogel formation via brush-first ring-opening metathesis polymerization followed by cross-coupling and ROMP-out.

4.3. GPC Acid Degradation Studies

In efforts to analyze the incorporation of PEG-MM into the BASP nanogel, additional GPC studies were performed with acid-degraded BASP nanogels. This approach allows to determine the identity of the polymerized bottle-brush polymer chain as well as find evidence on whether ROMP-out occurred. Figure 18 shows the GPC traces of acid-degraded N = 10 BASP nanogels with m =

0, 5, and 10 BASP nanogels shifted to a lower MW confirms successful degradation. In particular, the m = 0 peak is located at the shoulder of the non-degraded m = 0 BASP nanogel indicating the regeneration of the parent bottle-brush polymer upon acid degradation.

The continuous shift towards a shorter retention time as m increases implies the incorporation of additional PEG-MM into the bottle-brush polymer. However, the difference in retention time between acid-degraded and non-degraded BASP nanogels becomes successively smaller for m = 5, 10, and 20 BASP nanogels suggesting that corresponding BASP nanogels contain a smaller number of cross-coupled bottle-brush polymers. In fact, the m = 20 peak overlaps with that of its non-degraded BASP nanogel implying that no substantial cross-coupling has occurred. This observation leads to the theory that increasing m increased the steric hindrance of one bottle-brush polymer cross-coupling with another bottle-brush polymer, which may disprove the ROMP-out theory as stated in 4.2. Gel Permeation Chromatography Studies.
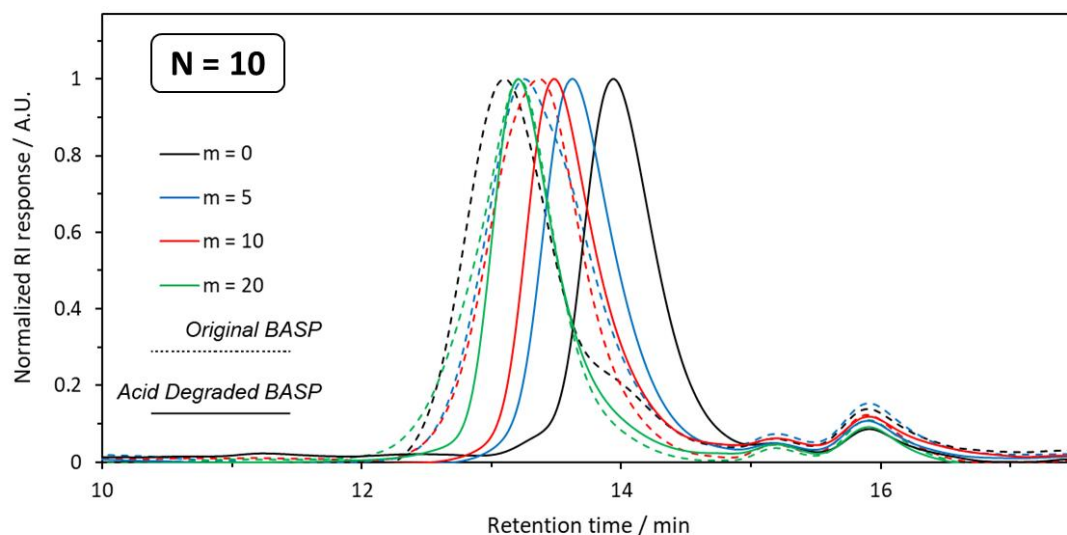
Figure 18. Refractive index GPC traces of TFA degraded and non-degraded N = 10 BASP nanogels using various amounts of PEG-MM.

The acid degradation of a BASP nanogel that involved ROMP-out was expected to regenerate the original bottle-brush polymer (corresponding to ineffective ROMP-out) as well as a

higher MW brush polymer formed by combination of ROMP-in and ROMP-out, as illustrated in Figure 19a and b. As a result, a bimodal mass distribution with one peak at a retention time similar to that of the unreacted bottle-brush polymer and a second peak at a shorter retention would provide strong evidence for ROMP-out. However, the absence of a shoulder peak corresponding to ineffective ROMP-out for m = 5, 10, and 20 BASP nanogels suggests the regeneration of a single high MW species that did not undergo ROMP-out (Figure 19c). In fact, the complete incorporation of cross-linker and PEG-MM before cross-linking successfully explains the decreasing extent of cross-coupling observed as the amount of PEG-MM is increased. In contrast, bottle-brush polymer formed via ROMP-out should result in BASP nanogels with similar levels of cross-coupling (i.e., steric hindrance) regardless of the amount of PEG-MM added as cross-coupling occurs before the incorporation of PEG-MM.
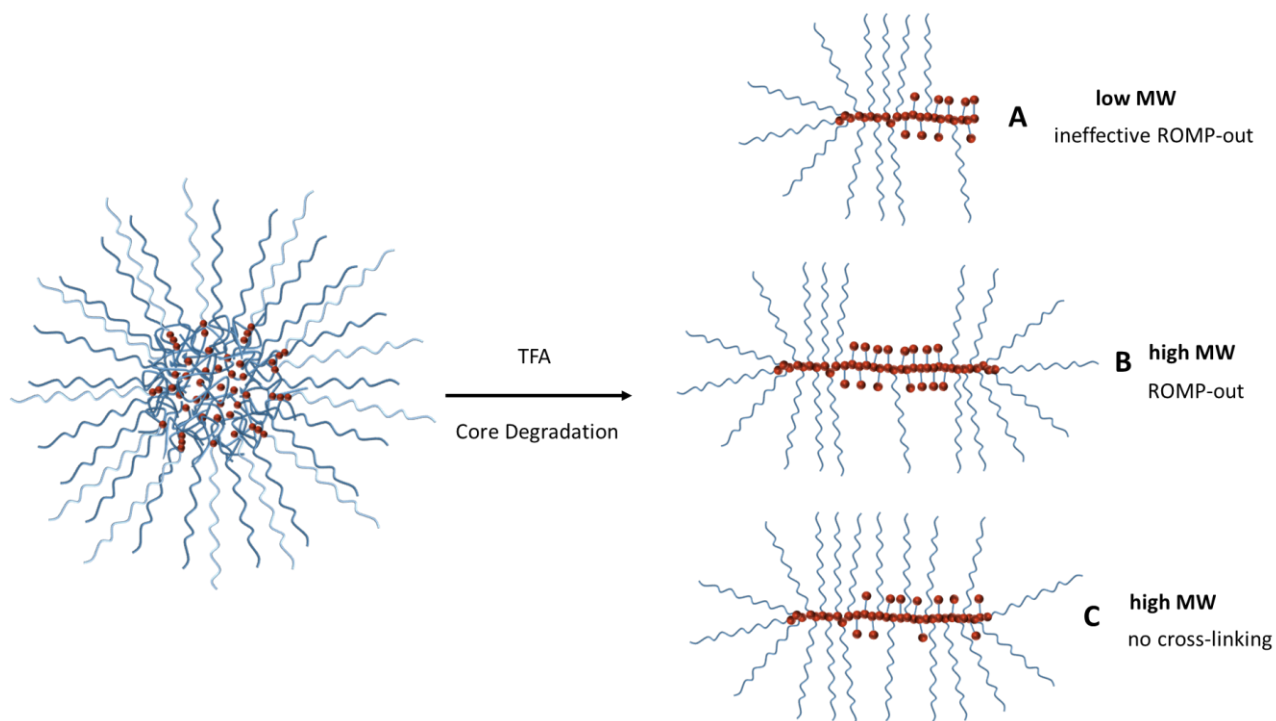

Figure 19. Schematic illustration of species regenerated from acid-triggered BASP nanogel degradation with a) representing bottle-brush polymer formed by ineffective ROMP-out, b) bottle-brush polymer formed via ROMP-out and c) bottle-brush polymer formed without ROMP-out.

The GPC traces obtained for acid-degraded N = 20 (Figure 20) and N = 30 (Figure 21) BASP nanogels confirm the trend observed for N = 10 BASP nanogels. In particular, the GPC peaks are continuously shifted towards a shorter retention time as m increases indicating a higher MW of the regenerated bottle-brush polymer. Notably, the GPC peak for the acid-degraded m = 20 BASP nanogel with N = 20 only overlaps with the right side of the corresponding non-degraded BASP nanogel peak suggesting that some cross-coupling has occurred to form higher MW species represented by the left side of the peak. The difference between the acid-degraded and non-degraded GPC peak becomes even larger for the N = 30 BASP nanogel implying increased cross-coupling of bottle-brush polymer. In general, this trend suggests that the extent of cross-coupling is strictly controlled by the ratio of cross-linker to macromonomer. Cross-linker incorporated into the bottle-brush polymer provides sites for cross-coupling, whereas the macromonomer introduces steric hindrance. Thus, adjusting the ratio of cross-linker to macromonomer offers potential in synthesizing BASP nanogels with precise control over the extent of cross-coupling and cross-linking.
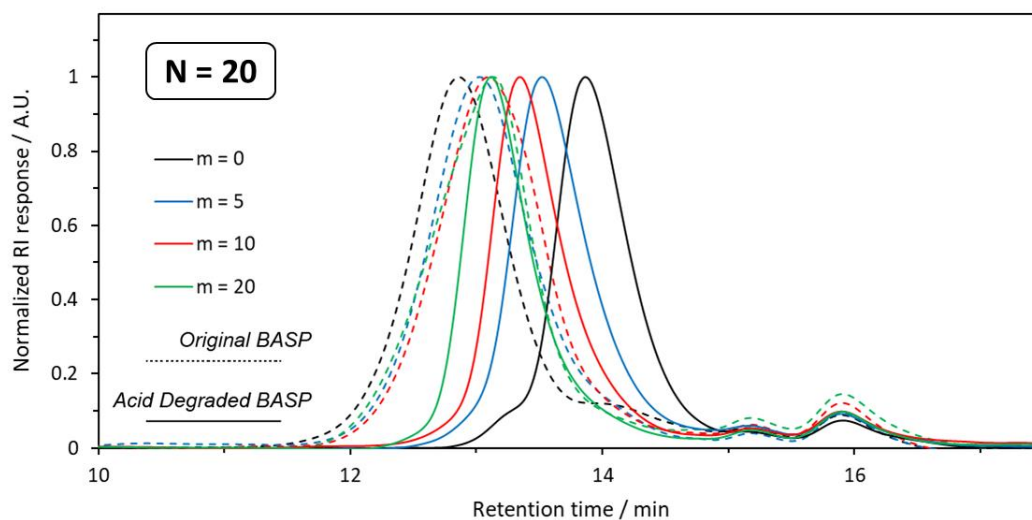
Figure 20. Refractive index GPC traces of TFA degraded and non-degraded N = 20 BASP nanogels using various amounts of PEG-MM.
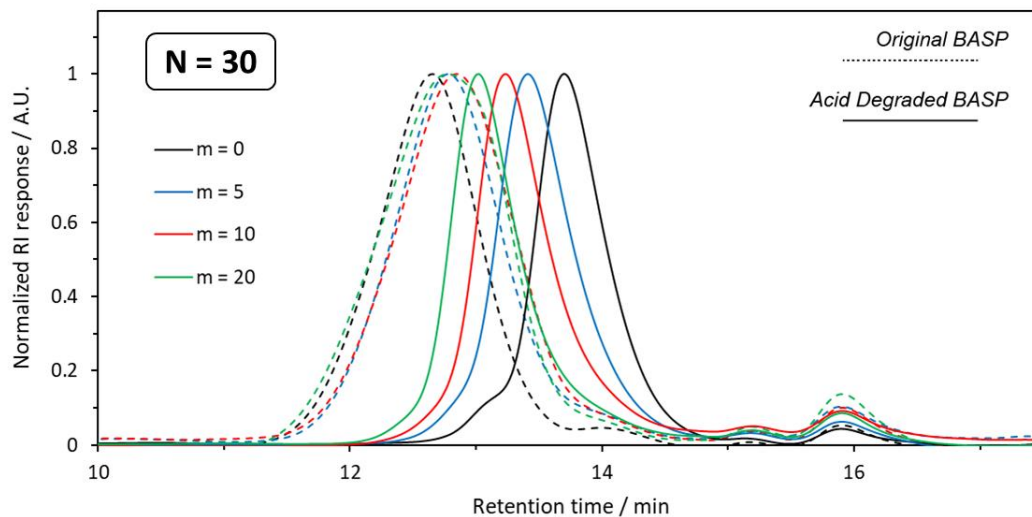
Figure 21. Refractive index GPC traces of TFA degraded and non-degraded N = 30 BASP nanogels using various amounts of PEG-MM.

4.4. Fluorescence Dye Loading Studies

The diffusion of a molecule in and out the BASP nanogel core was analyzed using fluorescein dye (Figure 23b) having a comparable size and hydrophobicity compared to common chemotherapeutic agents such as doxorubicin. BASP nanogels were exposed to a concentrated fluorescein dye solution. The relative hydrophobicity of the cross-linked core was expected to trigger the diffusion of dye into the core and effectively load the BASP nanogels. Excess dye not entrapped in the nanogel core was removed via dialysis against nanopure water before collecting fluorescence emission measurements. The obtained fluorescence intensities showed a great variability regardless of the amount of cross-linker and PEG-MM. The substantial decrease in peak intensity observed for N = 20 BASP nanogels (Figure 22b) compared to N = 10 (Figure 22a) and N = 30 (Figure 22c) was not reproducible. In fact, the two other sets tested (Figure S1 and S2) show no particular trend and disagree with the values shown in Figure 22.
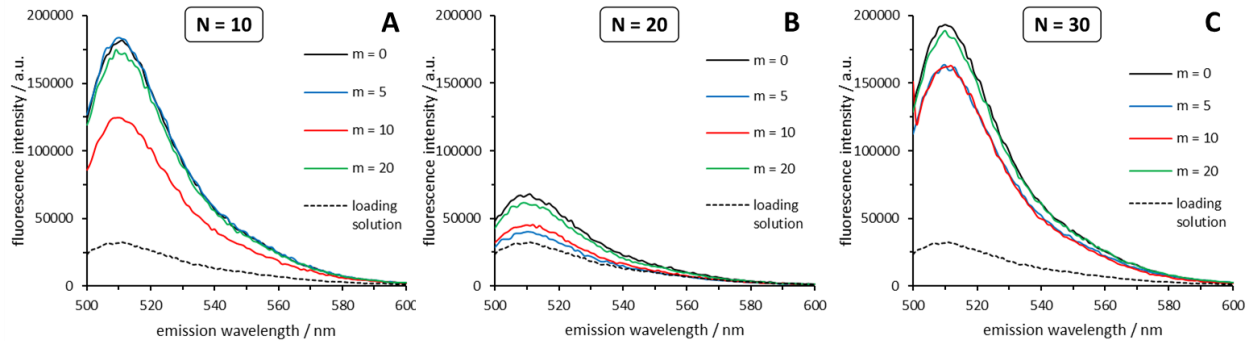
Figure 22. Trial set 1 of fluorescence emission intensities obtained for fluorescein-loaded BASP nanogels with (a) N = 10, (b) N = 20, and (c) N = 30 using an excitation wavelength of 490 nm.

The variability in the obtained results may be attributed to the sample preparation and loading procedure. After dialysis, remaining solvent is typically removed to obtain dry dye-loaded BASP nanogels with known mass. In a subsequent step, the BASP nanogels are reimmersed into water before determining the fluorescence intensity. However, dried BASP nanogels do not readily reimmerse back into solution suggesting possible entanglement due to lyophilization. As a result, the samples were sonicated in an attempt to break up potential entanglement and facilitate reimmersion. This step may negatively affect the reproducibility as it may trigger the diffusion of dye out of the nanogel core. Furthermore, it is unclear as to what extent the entanglement is broken up via sonication. N = 30 BASP nanogels with m = 0, in particular, did not fully go back into solution even after extensive sonication possibly due to a large hydrophobic cross-linked core.

While dye loading procedure was not reproducible, all BASP nanogels exhibit a higher fluorescence intensity than the respective fluorescein dye loading solution (Figure 22 dashed line). As the amount of fluorescein entrapped in the BASP nanogel cannot exceed the starting amount present in the loading solution, these results suggest a fluorescence enhancing effect caused by the BASP nanogel.

In order to test this theory, the fluorescence intensity of fluorescein dye solutions was tested before and after the addition of a small aliquot of BASP nanogel solution resulting in a decrease in

intensity in contrast to the observed increase for dye-loaded BASP nanogels. This observation provides strong evidence that the fluorescence enhancement effect can be attributed to the successful loading of dye into the BASP. In fact, the spatial entrapment of chromophores may result in Förster resonance energy transfer (FRET). Typically, an excited donor chromophore transfers energy to an acceptor chromophore via dipole-dipole coupling. However, the rate of energy transfer decreases as the distance between the donor and acceptor chromophore increases making FRET a powerful tool to analyze the interactions between molecules.[59] While no separate donor and acceptor chromophores were used in this study, FRET can also occur between similar chromophores. As shown in Figure 23a, the absorbance and emission spectra of fluorescein exhibit a spectral overlap between 480 and 530 nm. Thus, the fluorescence emission in this region may trigger the excitation of other fluorescein molecules nearby via FRET explaining the fluorescence intensity enhancing effect of dye-loaded BASP nanogels.
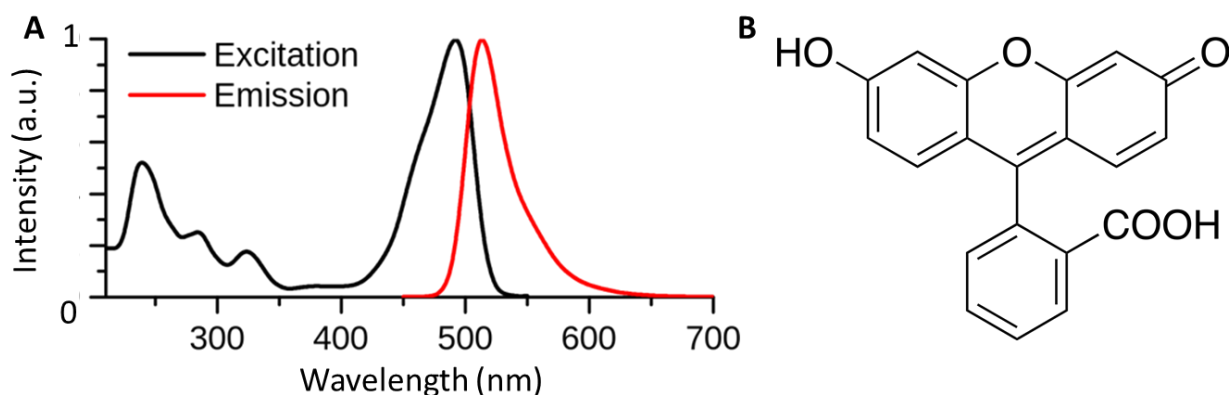
Figure 23. (a) Fluorescein absorbance and emission spectrum showing a spectral overlap that can cause FRET. Reproduced from https://commons.wikimedia.org/wiki/File:Fluorescein_spectra.svg. (b) Chemical structure of protonated fluorescein molecule.

This effect may potentially enable the direct comparison of loading efficiencies between different BASP nanogels directly in the dye loading solution. The extent to which FRET occurs provides valuable information about the amount of fluorescein dye entrapped inside the BASP

nanogel. Furthermore, the use of a more specific acceptor-donor pair such as rhodamine and fluorescein would enhance the quality of this study. Conjugation of the acceptor chromophore rhodamine to the macromonomer allows to monitor the diffusion of fluorescein in and out the BASP via FRET. Additionally, ICP-MS studies would provide additional information about the accessibility of the core for small molecules by quantifying how much left-over initiator Ru is removed from nanogel core through ROMP termination.
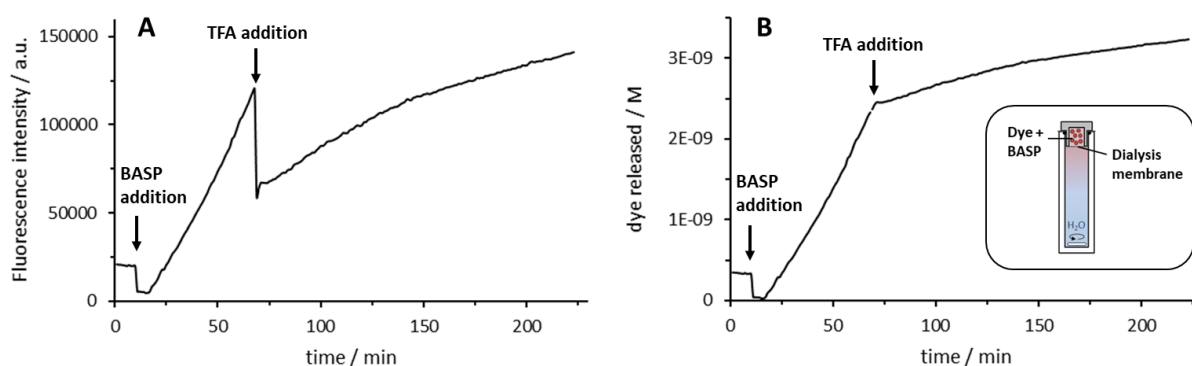
4.5. Fluorescence Dye Release Studies

The ability of BASP nanogels to release dye molecules upon acid-triggered core degradation was attempted using BASP nanogels that had been exposed to a concentrated fluorescein dye solution. The diffusion of fluorescein dye out of the BASP nanogel was evaluated by filling a cuvette cap with a dye-loaded BASP nanogel and wrapping a dialysis membrane with a pore size smaller than that of the BASP nanogel around it similar to the procedure described by Wuttke et al.[60] Fluorescein dye not entrapped in the BASP nanogel will diffuse through the dialysis membrane into the cuvette allowing the measurement of the fluorescence intensity of the released dye.

Figure 24a shows the dye release from a N = 20 BASP nanogel with m = 5 using an emission intensity of 510 nm and an excitation wavelength of 438 nm. After addition of the dye-loaded BASP nanogel to the cuvette cap (Figure 24b inset), the fluorescence intensity immediately increased in a linear fashion corresponding to the diffusion of dye out of the BASP nanogel even without core degradation. This observation suggests that the fluorescein dye is rather loosely associated to the BASP nanogel rather than tightly entrapped inside the core as expected for BASPs with the dye conjugated to the macromonomer.

The degradation of the BASP nanogel was triggered by lowering the pH to 2 through the addition of TFA. As shown in Figure 24a, the addition of TFA resulted in an immediate drop in fluorescence intensity correlated to the protonation of fluorescein negatively affecting its quantum yield and emission spectrum.[61] As a result, two different standard calibration curves were obtained for neutral pH as well as pH 2 to correct for this effect and convert fluorescence intensities into corresponding concentrations. The corrected graph (Figure 24b) shows an increase in fluorescein dye concentration after the addition of the dye-loaded BASP nanogel. However, the release of fluorescein dye levels off directly upon addition of TFA.

While it was suspected that degrading the BASP nanogel would result in an immediate complete release of fluorescein dye, the core degradation may not be fast enough relative to the time-scale studied in this experiment. Previous studies have shown that the core degradation of regular BASPs with acetal cross-linker at pH 4 is rather slow taking several days for complete degradation.[49] Assuming a mostly intact BASP nanogel in this study, the decrease in fluorescein dye release may be correlated to the protonation of the fluorescein as a result of the lower pH. Protonating fluorescein increases its hydrophobic characteristics enhancing its affinity for the hydrophobic cross-linked BASP nanogel core.

Figure 24. Dye release study of a fluorescein-loaded $N = 20$, $m = 5$ BASP nanogel showing (a) fluorescence intensities at 510 nm using an excitation wavelength of 438 nm and (b) converted fluorescein concentration over time. Inset: experimental setup showing dye-loaded BASP in cuvette cap with a dialysis membrane wrapped around. BASP nanogel solution was added to the cap system after 10 min followed by the addition of TFA after 70 min.

While this study provides insights into the interactions between fluorescein dye and the BASP nanogel, comparison between different BASP nanogel architectures would be helpful in evaluating their affinity for fluorescein dye. A more practically relevant approach to analyze the dye release ability is based on conjugating the dye or a dye-labelled drug molecule directly to the macromonomer. Thus, the incorporation of dye into the BASP nanogel can be ensured. Furthermore, this would allow to mimic the drug release under physiological conditions.

5. Conclusion

The synthesis of BASP nanogels via simultaneous addition of an acetal cross-linker and PEG-macromonomer after brush-first ROMP was successfully demonstrated. GPC analysis indicates the incorporation of PEG-MM into the BASP nanogel core. However, the heteropolymerization of cross-linker and macromonomer to the bottle-brush polymer increases steric hindrance during cross-linking resulting in BASP nanogels with lower MW compared to regular BASP. This effect diminishes as large amounts of PEG-MM (m = 20) is added during the cross-linking step suggesting the occurrence of an additional mechanistic step after cross-coupling. This proposed ROMP-out step involves the polymerization of unconverted PEG-MM to the still active initiator inside the BASP nanogel. This theory is confirmed by GPC acid degradation studies showing the regeneration of high MW species rather than the parent bottle-brush polymer. These results show potential for testing the copolymerization with low MW molecules instead of PEG-MM that can help control the properties of the BASP nanogel core.

In general, varying the amount of cross-linker suggests a saturation level of PEG-MM that can be incorporated before cross-coupling occurs related to the ratio of PEG-MM to cross-linker. However, additional characterization via small angle X-ray scattering would be helpful to analyze the composition of the BASP nanogel shell and core. Fluorescence studies suggest the successful diffusion and accumulation of fluorescein dye into the BASP nanogel. Nevertheless, further studies will be necessary to improve the reproducibility and allow quantitative comparison between different BASP architectures.

6. Bibliography

(1)   World Health Organization (WHO), Cancer Prevalence - Fact Sheet. **2017**.

(2)   American Cancer Society. *Cancer Facts and Figures*. **2017**.

(3)   Corrie, P. G. *Medicine (Baltimore). **2007**, *36* (1), 24–28.

(4)   Byrne, J. D.; Betancourt, T.; Brannon-Peppas, L. *Adv. Drug Deliv. Rev.* **2008**, *60* (15), 1615–1626.

(5)   Maeda, H. *Adv. Enzyme Regul.* **2001**, *41* (00), 189–207.

(6)   Prabhu, R.; Patravale, V.; Joshi, M. *Intern Journ of Nanomed* **2015**, *10*, 1001–1018.

(7)   Carmeliet, P.; Jain, R. K. *Nature* **2000**, *407*, 249–257.

(8)   Nakamura, Y.; Mochida, A.; Choyke, P. L.; Kobayashi, H. *Bioconjug. Chem.* **2016**, *27* (10), 2225–2238.

(9)   Jain, R. K. *Cancer Res.* **1987**, *47* (17), 3039–3051.

(10)   Matsumura, Y.; Maeda, H. *Cancer Res.* **1986**, *6* (December), 6387–6392.

(11)   Wakaskar, R. R. *Int. J. Drug Dev.* **2017**, *9* (2), 37–41.

(12)   Upreti, M.; Jyoti, A.; Sethi, P. *Transl. Cancer Res.* **2013**, *2* (4), 309–319.

(13)   Low, P. S.; Kularatne, S. A. *Curr. Opin. Chem. Biol.* **2009**, *13* (3), 256–262.

(14)   Daniels, T. R.; Delgado, T.; Helguera, G.; Penichet, M. L. *Clin. Immunol.* **2006**, *121* (2), 159–176.

(15)   Minko, T. *Adv. Drug Deliv. Rev.* **2004**, *56* (4), 491–509.

(16) Iinuma, H.; Maruyama, K.; Okinaga, K.; Sasaki, K.; Sekine, T.; Ishida, O.; Ogiwara, N.; Johkura, K.; Yonemura, Y. *Int. J. Cancer* **2002**, *99* (1), 130–137.

(17) Kobayashi, T.; Ishida, T.; Okada, Y.; Ise, S.; Harashima, H.; Kiwada, H. *Int. J. Pharm.* **2007**, *329* (1–2), 94–102.

(18) Drummond, D. C.; Hong, K.; Park, J. W.; Benz, C. C.; Kirpotin, D. B. *Vitam Horm* **2000**, *60*, 285–332.

(19) Van Sluis, R.; Bhujwalla, Z. M.; Raghunand, N.; Ballesteros, P.; Alvarez, J.; Cerdán, S.; Galons, J. P.; Gillies, R. J. *Magn. Reson. Med.* **1999**, *41* (4), 743–750.

(20) Pelicano, H.; Martin, D. S.; Xu, R.-H.; Huang, P. *Oncogene* **2006**, *25* (34), 4633–4646.

(21) Saito, G.; Swanson, J. A.; Lee, K. D. *Adv. Drug Deliv. Rev.* **2003**, *55* (2), 199–215.

(22) Cheng, R.; Meng, F.; Deng, C.; Klok, H. A.; Zhong, Z. *Biomaterials* **2013**, *34* (14), 3647–3657.

(23) Whetten, J. L.; Williamson, P. C.; Heo, G.; Varnhagen, C.; Major, P. W. *Nat. Rev.* **2016**, 485–491.

(24) Goodwill, P. W.; Saritas, E. U.; Croft, L. R.; Kim, T. N.; Krishnan, K. M.; Schaffer, D. V.; Conolly, S. M. *Adv. Mater.* **2012**, *24* (28), 3870–3877.

(25) Kim, B. H.; Hackett, M. J.; Park, J.; Hyeon, T. **2014**.

(26) Choi, S. J.; Lee, J. K.; Jeong, J.; Choy, J. H. *Mol. Cell. Toxicol.* **2013**, *9* (3), 205–210.

(27) Ehlerding, E. B.; Chen, F.; Cai, W. *Adv. Sci.* **2015**, *3* (2), 1–8.

(28) Bobo, D.; Robinson, K. J.; Islam, J.; Thurecht, K. J.; Corrie, S. R. *Pharm. Res.* **2016**, *33*

(10), 2373–2387.

(29)   Petersen, G. H.; Alzghari, S. K.; Chee, W.; Sankari, S. S.; La-Beck, N. M. *J. Control. Release* **2016**, *232*, 255–264.

(30)   Mc Carthy, D. J.; Malhotra, M.; O'Mahony, A. M.; Cryan, J. F.; O'Driscoll, C. M. *Pharm. Res.* **2015**, *32* (4), 1161–1185.

(31)   Colson, Y. L.; Grinstaff, M. W. *Adv. Mater.* **2012**, *24* (28), 3878–3886.

(32)   Liao, L.; Liu, J.; Dreaden, E. C.; Morton, S. W.; Shopsowitz, K. E.; Hammond, P. T.; Johnson, J. A. *J. Am. Chem. Soc.* **2014**, *136*, 11–14.

(33)   Barnes, J. C.; Bruno, P. M.; Nguyen, H. V. T.; Liao, L.; Liu, J.; Hemann, M. T.; Johnson, J. A. *J. Am. Chem. Soc.* **2016**, *138* (38), 12494–12501.

(34)   Rabanel, J. M.; Hildgen, P.; Banquy, X. *J. Control. Release* **2014**, *185* (1), 71–87.

(35)   Nguyen, H. V. T.; Chen, Q.; Paletta, J. T.; Harvey, P.; Jiang, Y.; Zhang, H.; Boska, M. D.; Ottaviani, M. F.; Jasanoff, A.; Rajca, A.; Johnson, J. A. *ACS Cent. Sci.* **2017**, *3* (7), 800–811.

(36)   Hadjichristidis, N.; Iatrou, H.; Pitsikalis, M.; Mays, J. *Controlled and Living Polymerizations*; 2006; Vol. 31.

(37)   Duro-Castano, A.; Movellan, J.; Vicent, M. J. *Biomater. Sci.* **2015**, *3* (10), 1321–1334.

(38)   Schaefgen, J. R.; Flory, P. J. *J. Am. Chem. Soc.* **1948**, *70* (8), 2709–2718.

(39)   Blencowe, A.; Tan, J. F.; Goh, T. K.; Qiao, G. G. *Polymer.* **2009**, *50* (1), 5–32.

(40)   Lutz, P.; Beinert, G.; Rempp, P. **1982**, *2797*, 2787–2797.

(41)	Matyjaszewski, K.; Tsarevsky, N. V. *Nat. Chem.* **2009**, *1* (4), 276–288.

(42)	Bazan, G. C.; Schrock, R. R.; Cho, H. N.; Gibson, V. C. *Macromolecules* **1991**, *24* (16), 4495–4502.

(43)	Saunders, R. S.; Cohen, R. E.; Wong, S. J.; Schrock, R. R. *Macromolecules* **1992**, *25* (7), 2055–2057.

(44)	Nuyken, O.; Pask, S. D. *Polymers.* **2013**, *5* (2), 361–403.

(45)	Ogawa, K. A.; Goetz, A. E.; Boydston, A. J. *J. Am. Chem. Soc.* **2015**, *137* (4), 1400–1403.

(46)	Gutekunst, W. R.; Hawker, C. J. *J. Am. Chem. Soc.* **2015**, *137* (25), 8038–8041.

(47)	Liu, J.; Burts, A. O.; Li, Y.; Zhukhovitskiy, A. V.; Ottaviani, M. F.; Turro, N. J.; Johnson, J. A. *J. Am. Chem. Soc.* **2012**, *134* (39), 16337–16344.

(48)	Burts, A. O.; Liao, L.; Lu, Y. Y.; Tirrell, D. A.; Johnson, J. A. *Photochem. Photobiol.* **2014**, *90* (2), 380–385.

(49)	Gao, A. X.; Liao, L.; Johnson, J. A. *ACS Macro Lett.* **2014**, *3* (9), 854–857.

(50)	Greenwald, R. B.; Pendri, A.; Conover, C. D.; Zhao, H.; Choe, Y. H.; Martinez, A.; Shum, K.; Guan, S. *J. Med. Chem.* **1999**, *42* (18), 3657–3667.

(51)	Johnson, J. A.; Lu, Y. Y.; Burts, A. O.; Xia, Y.; Durrell, A. C.; Tirrell, D. A.; Grubbs, R. H. *Macromolecules* **2011**, *43* (24), 10326–10335.

(52)	Wicki, A.; Witzigmann, D.; Balasubramanian, V.; Huwyler, J. *J. Control. Release* **2015**, *200*, 138–157.

(53)	Oh, J. K.; Drumright, R.; Siegwart, D. J.; Matyjaszewski, K. *Prog. Polym. Sci.* **2008**, *33* (4),

448–477.

(54)   Moore, J. C. *J. Polym. Sci. Part A Gen. Pap.* **1964**, *2* (2), 835–843.

(55)   Striegel, A. M.; Yau, W. W.; Kirkland, J. J.; Bly, D. D. *SIZE-EXCLUSION LIQUID CHROMATOGRAPHY Practice of Gel Permeation and*, 2nd ed.; John Wiley & Sons, 2009.

(56)   M. Rubinstein; R.H. Colby. Oxford Press 2009.

(57)   Williams, R. T.; Bridges, J. W. *J. Clin. Pathol.* **1964**, *17* (4), 371–394.

(58)   Lakowicz, J. R. *Instrumentation for Fluorescence Spectroscopy*; 2006.

(59)   Piston, D. W.; Kremers, G. J. *Trends Biochem. Sci.* **2007**, *32* (9), 407–414.

(60)   Wuttke, S.; Braig, S.; Preiß, T.; Zimpel, A.; Sicklinger, J.; Bellomo, C.; Rädler, J. O.; Vollmar, A. M.; Bein, T. *Chem. Commun.* **2015**, *51* (87), 15752–15755.

(61)   Lee, D. H.; Sung, H. J.; Han, D. W.; Lee, M. S.; Ryu, G. H.; Aihara, M.; Takatori, K.; Park, J. C. *Yonsei Med. J.* **2005**, *46* (2), 268–274.
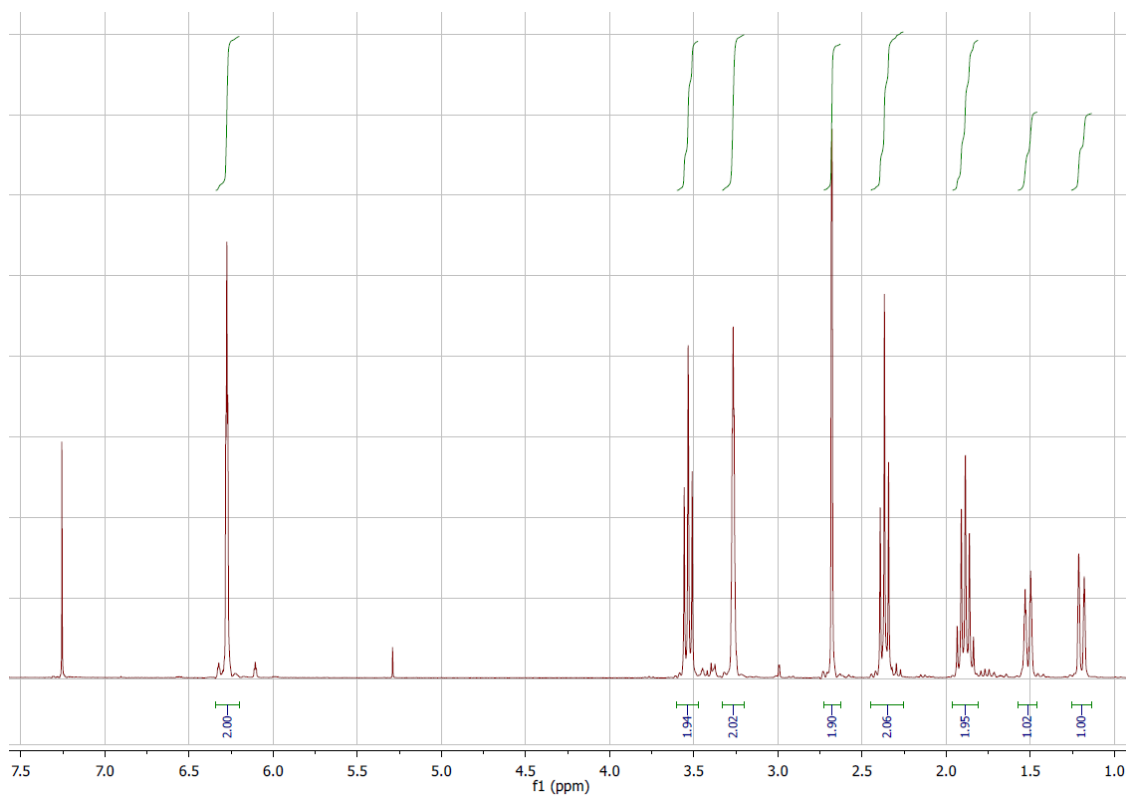
7. Appendix
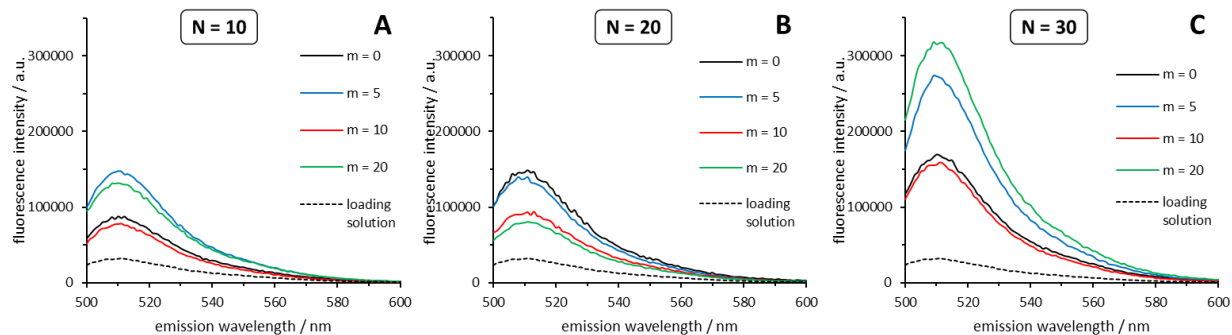
Figure S1. Fluorescence emission intensities obtained for fluorescein-loaded BASP nanogels with (a) N = 10, (b) N = 20, and (c) N = 30 using an excitation wavelength of 490 nm.
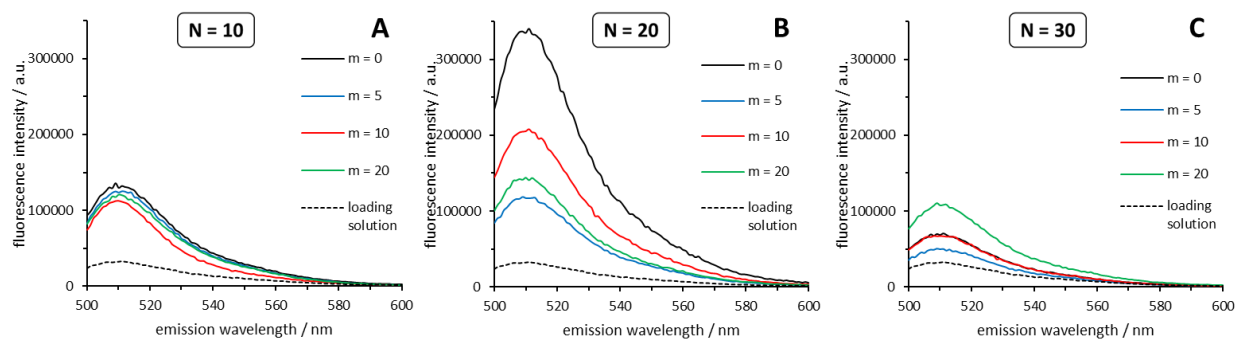
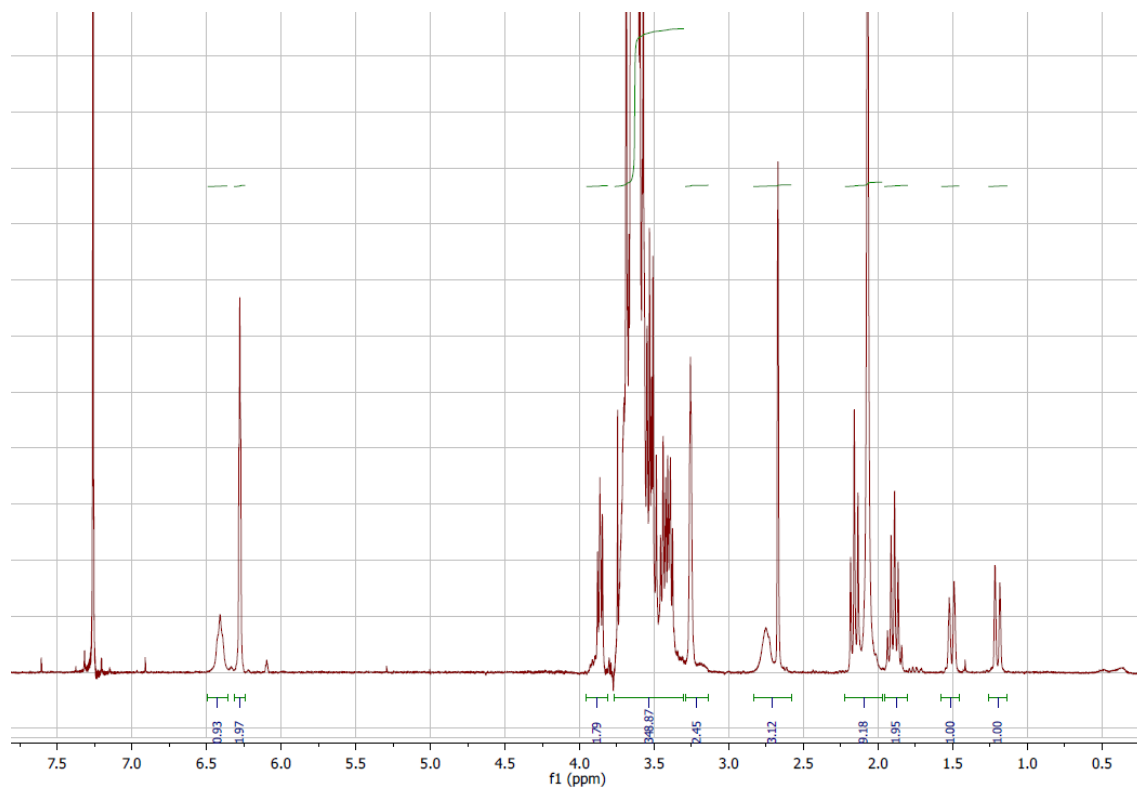**Figure S2.** Fluorescence emission intensities obtained for fluorescein-loaded BASP nanogels with (a) N = 10, (b) N = 20, and (c) N = 30 using an excitation wavelength of 490 nm.

Figure S3. ^{1}H NMR spectrum of **1** in CDCl$_3$.
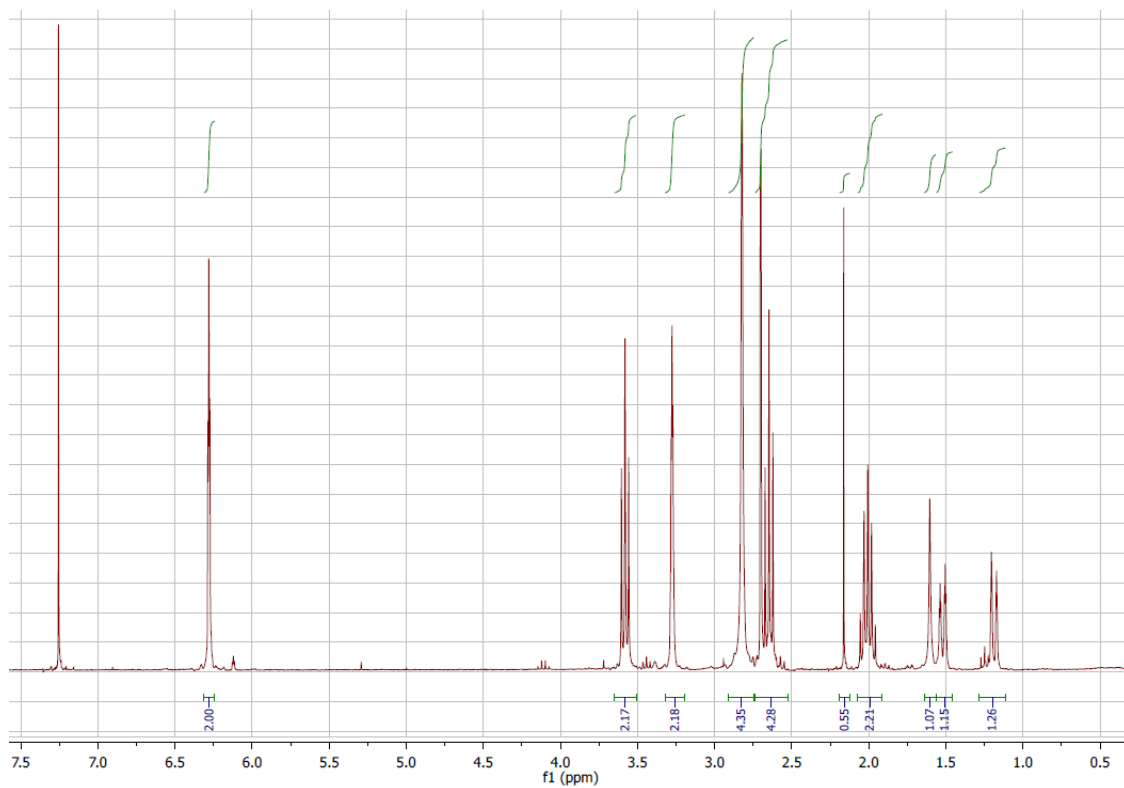
Figure S4. ^{1}H NMR spectrum of **2** in CDCl$_3$.

Grundler 51

Figure S5. ^{1}H NMR spectrum of **PEG-MM** in CDCl$_3$.